Free-standing, axially-symmetric diffraction gratings for neutral matter-waves: experiments and fabrication

Thomas Reisinger

Dissertation

submitted to the Department of Physics and Technology
in partial fulfillment of the requirements for the degree of

Philosophiae Doctor (PhD)

at the
University of Bergen

August 2011

Preface

This thesis, which is submitted to the Department of Physics and Technology at the university of Bergen for the degree of Philosophiae Doctor (PhD), consists of two parts. The first is a treatise which summarizes and extends the contents of four articles published in international, peer-reviewed journals during the 4-year-long PhD-project period and one article to be submitted to an international peer-reviewed journal. The second part of this thesis is a reprint of these five articles.

The project period was spent at three different institutions. During the first five months (1st Sep. 2007 - 17th Feb. 2008) the Poisson spot and focusing experiments were carried out at the Graz University of Technology using the helium scattering apparatus called 'Magie'. In the period Feb. 17th 2008 to May 15th 2008 'Magie' was moved and successfully setup at the university of Bergen. After that the candidate spent 11 months (May 15th 2008 - Apr. 4th 2009) at the NanoStructures Laboratory at the Massachusetts Institute of Technology (MIT) as a visiting student to develop a fabrication process for free-standing silicon-nitride zone-plates (Paper C). The remaining two-and-a-half years were spent at the university of Bergen where one of the main priorities was the setup of a nano-structuring facility similar to the one at MIT.

Supervisor:	Prof. Bodil Holst University of Bergen, Bergen, Norway
Co-Supervisor:	Prof. Henry I. Smith Massachusetts Institute of Technology, Cambridge, USA

Acknowledgements

Many have contributed to my PhD project in word and deed, and the following paragraphs can hardly be complete. So let me first thank everyone who has helped me in one or the other way throughout these four years.

First I would like to express my gratitude to Prof. Bodil Holst for being a great supervisor, entrusting me with much responsibility and giving me a good deal of freedom in my research. Throughout the project she was always ready to listen and provide motivational words when needed. I would also like to thank my co-supervisor Prof. Hank Smith for accepting me as a visiting student at one of the greatest scientific institutions on the planet. The eleven months at MIT have been an extremely fruitful and enjoyable period in my life.

I am very thankful for the many exciting discussions and fruitful collaboration with Gianangelo Nino Bracco. I hope we will be able to publish many more articles together!

Next there is Sabrina Eder who has been a great office mate, friend and fellow experimentalist. Herbert Reingruber who helped with moving the helium-beam apparatus MaGiE to Norway and getting me through the first few months in Norway. The importance of feeling welcome in a new place should never be underestimated. In this respect I would also like to thank Jenny Luneng, Sigrid Meyer, Andreas Samnøy, Christian Bergfjord and Hege Erdal - Hege additionally for helping me understand the immense intricacies of quantum field theory. I also want to thank Bjørn Samelin for help in many matters but especially regarding the use of MaGiE.

For allowing me to stay and keep an office at Graz university of technology during the initial 5 months of my PhD I want to thank Prof. Wolfgang Ernst.

Martin Greve I would like to thank as one of my first Master students and for becoming a good friend. Furthermore I want to acknowledge my other two master students Selda Ekiz and Eivind Johanessen who have worked with me on a new field ionization setup.

Kåre Slettebakken and Rachid Maad helped greatly with the laboratory move from Graz. I also want to acknowledge the professional support of the workshop at the physics department provided by Kåre, Roald Langøen, Leif Egil Sandnes, Charles Sebastiampillai and Svein Midtun.

Furthermore I want to thank the administration at UiB's physics department. In particular Gjert Furhovden for his patience with the countless orders and his help with setting up the new nano-structuring laboratory. In this respect I also acknowledge the help of Sverre Seth.

At MIT I want to thank all my coworkers at the NanoStructures Laboratory. Especially Jim Daley for being the professional lab engineer he is and always having some friendly words to offer. Mark Mondol for patiently building up my knowledge on electron-beam lithography and many motivating, enjoyable conversations. I am thankful to Prof. Karl Berggren, for being a great source of motivation and in particular for reading and commenting the Poisson-spot manuscript. I was lucky to share an office with Jie Sun and Simon Schuster, who especially supported my late night fabrication sessions on many occasions. Further there is Tom O'Reilly and Corey Fucetola who contributed particularly to this thesis by working with me on the Mach Zehnder interferometer. Tom also taught me about the Lloyds Mirror interferometer setup. Tim Savas, Sidney Tsai and Trey Holzwarth offered me patient advice on fabrication issues many times. Amil Patel I want to thank in particular for providing the free-standing discs that were used in the Poisson-spot experiment. Juan Ferrera and Feng Zhang provided many important hints on the Raith 150 and spatial-phase-locked electron-beam lithography. I am grateful to Orit Shamir for always being up for a cup of tea and flirting in general. Deborah Morecroft I should thank for taking the time to teach me about etching silicon-nitride membranes and how to best handle them. Donny Winston I should thank for letting me join his journal club on templated self-assembly. Finally, I want to thank Lin Lee Cheong for the time that we shared together.

I am deeply indebted and grateful to my parents Jochen and Annemarie. I could not have gotten here without their never-failing support. Also I am grateful to my brother Andi and his Anna among many things but with regard to this thesis for providing a couch in Vienna on countless occasions. Similarly I am thankful to my brother Christoph, his wife Sandra and my nephew and god-son Sebastian.

Finally I want to thank Bergens Research Foundation and Trond Mohn for providing the necessary funds for this doctoral project.

List of Papers

Paper A	Poisson's spot with molecules. T. Reisinger, A. A. Patel, H. Reingruber, K. Fladischer, W. E. Ernst, G. Bracco, H. I. Smith, and B. Holst. *Phys. Rev. A*, 79(5):053823, 2009. *Nature* Research Highlights 459, 7246 p.486 (2009).
Paper B	Particle-wave discrimination in poisson spot experiments. T. Reisinger, G. Bracco, and B. Holst. *New Journal of Physics*, 13(6):065016, 2011.
Paper C	Neutral atom and molecule focusing using a Fresnel zone plate. T. Reisinger and B. Holst. *Journal of Vacuum Science and Technology B*, 26:2374–2379 , 2008.
Paper D	Free-standing silicon-nitride zoneplates for neutral-helium microscopy. T. Reisinger, S. Eder, M. M. Greve, H. I. Smith, and B. Holst. *Microelectronic Engineering*, 87(5-8):1011 – 1014, 2010.
Paper E	Virtual-source size of a supersonic-expansion deuterium (D_2) beam. T. Reisinger, M. M. Greve, S. Eder, G. Bracco, B. Holst. To be submitted to *Physical Review A*.

Abstract

Since de Broglie's famous postulation of the wave-nature of material particles and its subsequent experimental verification, it is known that atoms and molecules behave like waves on a small scale. The investigation of matter waves is a fundamental topic in quantum mechanics. Furthermore, matter waves have many applications in a number of scientific fields. For example they are used to investigate materials by studying the diffraction of atoms (Helium Atom Scattering) or electrons (Low-energy electron-diffraction) from the material's surface. The topic of this thesis has been to make nano-structured optical elements for matter-waves and use them in a number of experiments. A major result of this thesis is the performance of the classical Poisson-spot experiment with neutral matter-waves. The Poisson-spot refers to the bright interference spot observed in the shadow of a circular obstacle. The experiment gave convincing evidence of the wave nature of light at the beginning of the 19^{th} century.

The first two articles (A&B) in this thesis are concerned with the Poisson-spot experiment for matter waves and its applications. The experiment was performed using low-energy deuterium molecules (normal D_2, 23.5 meV), which is described in the first article. In the second article the feasibility of using the Poisson-spot experiment to demonstrate the wave-nature of large molecules is studied. The wave properties of large molecules are an important topic in current research. The remaining three articles are concerned with Fresnel zone-plates. Fresnel zone-plates are axially symmetric diffraction gratings that can be used to focus waves. Loosely formulated the relationship between Fresnel zone-plates and the circular object in the Poisson-spot experiment is the same as the relationship between multiple-slit gratings and a single straight edge. Paper C studies the application of microscopy with neutral atoms and molecules and the limitations of focusing matter waves with zone plates. The fabrication of the nano-structured free-standing zone-plates using electron-beam lithography is the topic of paper D. A second, new application of Fresnel zone-plates is introduced in paper E: There a zone plate is used for a direct size measurement of the so-called virtual source in a supersonic expansion.

The main-result from the Poisson-spot experiment was the observation of the Poisson spot with a molecular-deuterium beam and the successful comparison of the collected experimental data with Fresnel-diffraction theory. The wave-length independence of the on-axis interference-condition in the Poisson-spot experiment and the weak constraints on angular alignment and position of the circular object led us to conclude that the Poisson spot is a good candidate for demonstrating the wave nature of larger molecules.

This idea is studied further in paper B, where among other things the feasibility of a Poisson-spot experiment with the fullerene molecule C70 is examined. The main conclusion from this article was that the wave-nature of a molecular-beam can be demonstrated in diffraction experiments with circular discs that have varying amount of intended edge-corrugation. This is because the dependence of the bright spot on the edge-corrugation in the particle-model is different than in the wave-model. The result for the C70 Poisson-spot was that the experiment would be very challenging with count rates as low as 10^{-4} s^{-1}. However, one possibility would be, due to the simplicity of the setup, to parallelize the experiment and measure the diffraction pattern behind many circular discs at once. This could be realized using the fabrication techniques discussed in chapter 4. Other applications of the Poisson spot could include the study of the Casmir-Polder potential, molecule-lithography and diffraction experiments with atom-lasers from Bose-Einstein condensates.

While Fresnel zone-plates can be used to focus any type of wave they suffer from strong chromatic aberration since their focal length is inversely proportional to wavelength. In the case of neutral atom and molecule focusing this is what limits resolution. Paper C presents the highest resolution helium transmission-images hitherto and results from the first focusing of molecular deuterium with a zone plate. In addition the paper discusses the resolution-limit and finds that with presently available techniques a minimal spot size of 300 nm full-width-at-half-maximum is feasible using a zone plate of 200 µm diameter and a beam with speed ratio of about 500.

The Fresnel zone-plates used to focus the supersonic-expansion beams need to be free-standing, since the low-energy atoms and molecules do not penetrate any material. In paper D an electron-beam lithography fabrication-process for free-standing zone-plates is presented. The process uses a 200-nm-thin layer of low-stress silicon-nitride for the material of the zone plates. The fabricated zone plates were tested in the supersonic-expansion beam apparatus. The transmission and first-order diffraction-efficiency are close to the theoretical prediction for the smaller 190 µm-diameter zone plates patterned with a single electron-beam write-field. A reduction to 70 % for the 388-µm-diameter zone-plate was observed which was attributed to stitching errors since it was stitched together from four write-fields. In chapter 4 additional unpublished results are presented on spatial-phase-locked electron-beam lithography, which aims at the reduction of stitching errors and other pattern-placement errors in electron-beam lithography.

Finally in paper E one of the fabricated zone plates in addition to a previously existing one is used to measure the virtual source-width of a molecular deuterium supersonic-expansion beam. The virtual source-width is a measure of the beam's temperature perpendicular to the beam axis. The beam's energy distribution along the beam axis is measured using the time-of-flight method. Data sets for source temperatures T_0=310 K and T_0=106 K were collected in the stagnation pressure ranges p_0=3-171 bar and p_0=3-131 bar, respectively. The measured parameters were compared to a simple model of the expansion which explicitly includes the coupling between translational and rotational degrees of freedom. The data generally corresponded very well to the model, except for the virtual source size which was systematically about 2/3 of the model's prediction. For the cold source-conditions the beam is increasingly heated due to condensation effects at increasing pressures, which results in a clear deviation from the model. This could be used to estimate the fraction of condensed molecules in the beam.

Contents

Chapter 1

Introduction

The topic of this thesis is diffraction of atoms and molecules from structures with axial symmetry. Diffraction experiments are a convenient way for demonstrating the wave nature of material particles, which is dictated by quantum mechanics. In fact convincing the scientific community of the wave nature of light was accomplished with a very simple diffraction experiment at the beginning of the 19^{th} century. It concerned the diffraction behind a circular object like a disc or a sphere. Wave-theory predicts that there is a bright spot at the center of the shadow of such an object due to positive interference of the waves (the so-called Poisson spot). The bright interference-spot can be intensified by increasing the number of concentric, circular edges, which is realized in Fresnel zone-plates.

The diffraction experiments in this thesis were all carried out on the same supersonic-expansion-beam apparatus which is tailored to both transmission and reflection atom-optics experiments. In this thesis only the transmission-configuration was used. The ultra-high-vacuum apparatus consists of 10 differential pumping stages. The first contains the beam source where deuterium or helium gas expands into high-vacuum via a 10-μm platinum-nozzle. For the diffraction experiments the circular-disc or Fresnel zone-plate was mounted inside one of the vacuum chambers on a semi-automated stage and thus aligned with the collimated beam. The diffraction images were measured by either scanning the limiting aperture of the electron-bombardment ionization-detector in the imaging plane, or stepping the entire detector in the horizontal direction across the beam. The apparatus is further equipped with a beam chopper for time-of-flight experiments, which allows the characterization of the beam's energy distribution.

Another large part of this thesis was the development of numerical simulations to explain the diffraction patterns. It started out as a model for calculating the Poisson-spot diffraction pattern from a spatially-incoherent source and taking the imperfections of the circular object into account (paper A). In paper B it was extended to include particle-wall interaction (van-der-Waals forces). Paper B in addition presents a classical particle simulation of the beam with the aim of distinguishing between particle and wave behavior of the beam. Papers C and D use simple geometrical arguments to explain chromatic aberration of zone-plate focusing, as well as transmission and diffraction efficiency. Finally, in paper E the Fresnel-diffraction simulation of the Poisson-spot experiment was extended to simulate a zone-plate focus based on the measured wavelength-distribution of the beam.

In this thesis papers A and B on the Poisson spot are discussed in chapter 2. The contents of paper C on neutral-atom microscopy are the topic of chapter 3. The aspects of zone-plate fabrication with some additional results on spatial-phase-locked electron-beam lithography are given in detail in chapter 4. The application of zone-plate focusing to characterizing a molecular deuterium supersonic-expansion beam is summarized in chapter 5.

Chapter 2

The Poisson-spot experiment with matter waves (Papers A&B)

In 1923 Louis de Broglie conjectured that material particles could be described as waves on a small scale, in analogy to the particles of the electro-magnetic field [21]. This laid an important part of the foundations of the so-far extremely successful quantum-mechanical description of the microscopic part of our universe. Experimental evidence for de Broglie's conjecture came soon after that, in form of the experiments by Davisson and Germer [20] were it was shown that electrons propagate like waves when they reflect off nickel crystals. The distinctive feature in the propagation of these electrons was a phenomenon called diffraction, which is most commonly used to distinguish between particle and wave. When reflected off or transmitted through a periodic structure whose period is of the same order as the wavelength of an object, this object will not propagate along straight-line paths after interaction with the periodic structure. De Broglie's conjecture insisted that a relativistically invariant wavelength for material particles would have to be of the form

$$\lambda = \frac{h}{p} \tag{2.1}$$

where h is Planck's constant and p is the particle's linear mechanical momentum. This wavelength was confirmed by Davisson and Germer. It was soon demonstrated that this wavelength would also determine the paths of larger particles such as atoms. Estermann and Stern for example were the first to diffract helium atoms from a lithium-flouride crystal [90].

Countless experiments have been performed since, where material particles behave as so-called matter waves. An intriguing and unresolved question however still remains today: Is there an upper limit to the size, mass or complexity of material particles that can be demonstrated to exhibit wave-properties? The first in a series of experiments that aim at the investigation of this question was a far-field diffraction experiment with C60 molecules (buckyballs) [3]. Several mechanisms that lead to decoherence, which refers to the loss of wave-properties, have been identified. For example, the collision with background gas-particles in a vacuum chamber can be a cause for the loss of spatial coherence [46]. Another mechanism is the decoherence by emission of thermal radiation, which has been demonstrated with C70 molecules [40]. The largest molecules for which the quantum-mechanical wave-behavior has been demonstrated so far comprise up to 430 atoms with a size of up to 6 nm and a mass of up to 6910 amu [34]. These experiments have been enabled by nano-structured diffraction gratings which have been fabricated using similar methods as presented in chapter 4.

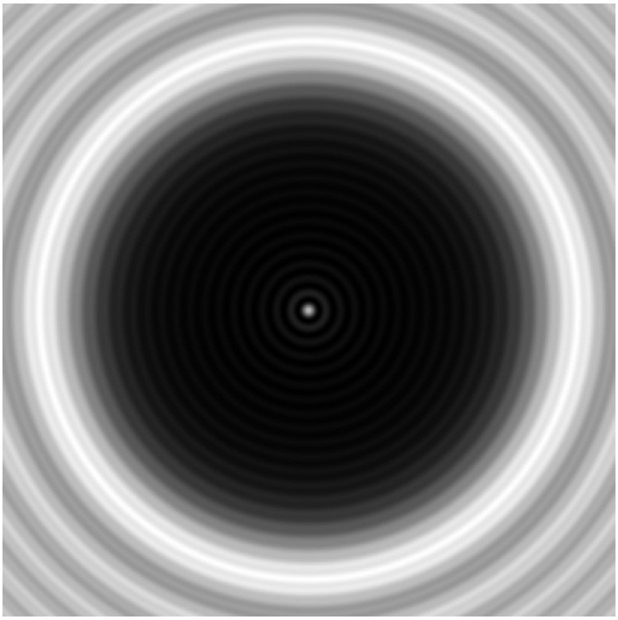

Figure 2.1: Poisson spot diffraction pattern.

At the beginning of the 19^{th} century the question if light is a particle or a wave occupied the minds of many great scientists. The ground-breaking experiment then was the Poisson-spot experiment as it clearly showed that light obeyed Fresnel's wave theory [32] as opposed to Newton's corpuscular theory of light [67]. It refers to the diffraction of waves in the shadow of a circular object. If the source of waves is sufficiently point-like and the distances between source, object and observer are chosen large enough, the waves will form a bright spot at the center of the shadow, called the Poisson spot or spot of Arago (see paper A). A first Poisson-spot-like diffraction pattern with matter waves has been observed in the 1-dimensional equivalent setup, namely a wire interferometer [68]. In paper A we have demonstrated the Poisson spot experiment with a free-jet-expansion beam of deuterium (D_2) molecules and a 2-dimensional nano-fabricated free-standing disc. We showed that the resulting diffraction pattern can be replicated closely using Fresnel's approximation of wave-propagation.

The question we have explored in paper B is if the Poisson-spot experiment can be used to demonstrate the wave-nature of larger molecules. We found that it is important to take into account the interaction of the free molecules with the shadow-casting disc as well as the unavoidable edge-corrugation of the disc. The dependence of the diffraction pattern on the latter is different for particle and wave which thus provides a new way to distinguish between the two behaviors.

This chapter is divided in three sections that each gives additional background for the experiments and simulations discussed in papers A and B. In the first section I have decided to include some of Fresnel's wave theory which is necessary to understand the diffraction model discussed in the section there-after. The final section gives an overview of the experimental apparatus, which was also used in the work presented in the remaining papers, and is therefore given from a general view point here.

2.1 Theoretical background

This section briefly summarizes some quantum mechanics and Fresnel's diffraction theory. It then goes on to explain how Fresnel's approximation can be used to calculate Poisson-spot diffraction patterns. The basic setup of a Poisson-spot experiment is shown in figure 2.2. A bright point source illuminates a circular disc suspended on some kind of support. At the center of the shadow, which is cast on a screen, a bright spot, the Poisson spot, can be observed. So the theoretical problem that needs to be solved is how to describe the intensity distribution on the screen.

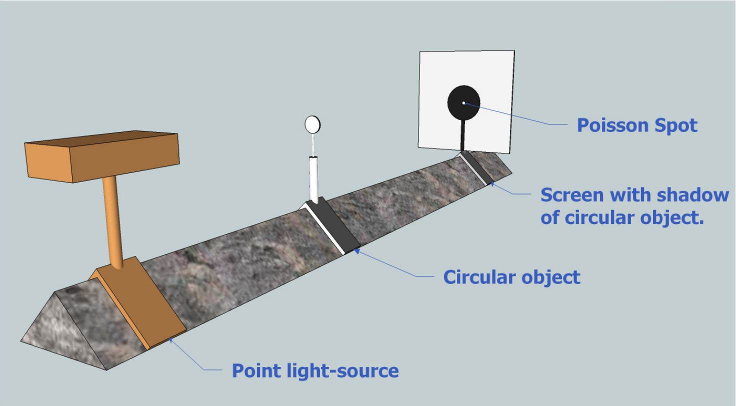

Figure 2.2: Schematic of a Poisson-spot experiment. A circular object is illuminated with a point source. At the center of the shadow of the circular object appears a bright spot due to diffraction. This is referred to as the Poisson spot or spot of Arago.

2.1.1 Quantum mechanics

In quantum mechanics a free particle is described by Schrödinger's famous wave equation[9]

$$\nabla^2 \psi = -\frac{2mE}{\hbar^2} \psi \tag{2.2}$$

where m is the particle's mass and E its kinetic energy. The absolute square amplitude $\left|\psi^2\right| = \psi\psi^*$ is proportional to the particle density. It is proportional to the probability that a particle will be observed at the given point in space. Using de Broglie's ansatz for the wavelength of a particle we can rewrite the equation as

$$\nabla^2 \psi = -(\frac{2\pi}{\lambda})^2 \psi \tag{2.3}$$

One can see that ψ is a stationary solution to the wave equation. In general the wave equation can be written as

$$\nabla^2 \Phi = \frac{1}{u^2} \frac{\partial^2}{\partial t^2} \Phi, \tag{2.4}$$

where u is the wave's group velocity. $\Psi(x,y,z,t)$ is a scalar wave field with (x,y,z,t) a point in space and time. With the plane-wave solution, namely,

$$\Phi(x,y,z,t) = \psi(x,y,z) e^{-\mathbf{i}\omega t} \tag{2.5}$$

and angular frequency $\omega = 2\pi f$ the stationary solution to the wave equation is given by:

$$\nabla^2 \psi = -(\frac{\omega}{u})^2 \psi = -(\frac{2\pi}{\lambda})^2 \psi \tag{2.6}$$

This we can then identify with Schrödinger's wave equation. In our case the beam propagates from source to detector and does not encounter any time-dependent fields. Also the beam-parameters like temperature and flow are kept constant. The stationary description is therefore adequate. Interestingly, unlike light particles which are described by the electro-magnetic field, material particles can exhibit diffraction in time in addition to the purely spatial diffraction we are concerned with in this work [12].

2.1.2 Fresnel diffraction

The Huyghens-Fresnel principle

In the previous section I have established that the D_2 molecular beam which we used in the Poisson-spot experiment can be described by a stationary wave. Fresnel's wave-theroy is therefore one option for representing the propagation of the deuterium molecules. The basis for this theory is the Huyghens-Fresnel Principle [44], which gives a recipe for calculating the intensity at a point P_1 that is illuminated by a wave-source at point P_0 (see figure 2.3). It states that all points on the unobstructed part of a wavefront serve as secondary sources with the same frequency as the original wave. To calculate the optical-field amplitude at an arbitrary point P_1 the contributions of all the secondary sources must be super-imposed taking into account their relative amplitudes and relative phases.

As an integral the total disturbance of the field at point P_1 can be stated as in the following equation:

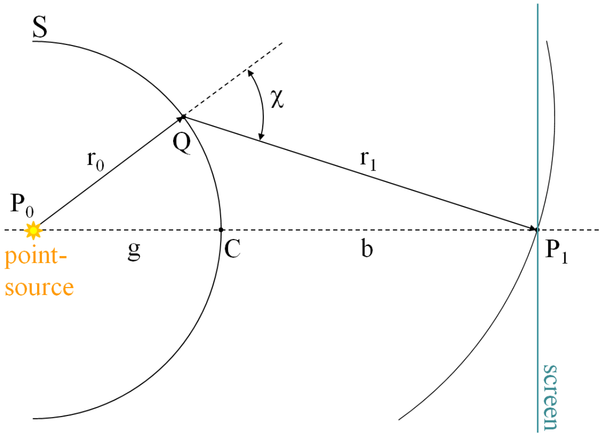

Figure 2.3: Notation for equation 2.7.

$$U(P_1) = \frac{Ae^{\mathbf{i}kr_0}}{r_0} \int\int_S \frac{e^{\mathbf{i}kr_1}}{r_1} K(\chi) dS. \qquad (2.7)$$

The notation is as indicated in figure 2.3. $K(\chi)$ is the so-called inclination factor. It represents the fact that the secondary wavelets do not propagate in the reverse direction. Kirchhoff found out that it is correctly given by:

$$K(\chi) = \frac{\mathbf{i}}{2\lambda}(1+\cos(\chi)) \qquad (2.8)$$

The spherical waves are represented by the fractions in equation 2.7 with the exponentials in the numerator. A is the amplitude of the source-wave.

Fraunhofer and Fresnel diffraction

Fresnel used the further simplification that the wavelength λ should be small with respect to the lateral dimensions of any obstacle or aperture obscuring the surface S and that they be small compared to the distances g=P$_0$C and b=CP$_1$. In this case it is advantageous to expand the values of r_0 and r_1 around g and b. If only the linear terms are significant in this expansion one speaks of Fraunhofer diffraction. This corresponds to the conditions [85]

$$g \to \infty, b \to \infty \qquad (2.9)$$

For Fraunhofer diffraction the wave-source is so far away that the incoming waves are plane waves and also the screen is so distant that the curvature of the spherical wavefronts close to the optical axis is negligible. Fresnel diffraction takes into account the quadratic terms of the expansion, so that the curvatures of the wavefronts are taken into account. The following rule-of-thumb ([44]) can be used to decide if Fresnel diffraction needs to be considered:

$$F = \frac{d^2}{l\lambda} \gtrsim 1 \tag{2.10}$$

The is sometimes referred to as the Fresnel number. l corresponds to the smaller of g and b. d is the largest lateral dimension of the aperture or obstacle. For the experimental setup in Paper A the Fresnel number was in the range of $F \approx 50-120$.

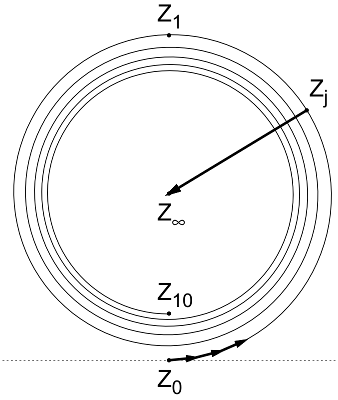

Figure 2.4: Vibration curve (after [44]). The arrow indicates the phasor corresponding to the solution of the Huyghens-Fresnel integral in equation 2.7 for a circular obstacle which blocks the first j Fresnel zones (see sectionsec:zoneplates). For a circular aperture the phasor always originates at Z_0 and ends at a point on the spiral corresponding to the edge of the circumference of the aperture.

The Poisson spot

To intuitively understand why the Huyghens-Fresnel principle leads to a bright spot in circular shadows, the Poisson spot, one can visualize the integral in equation 2.7 with the curve displayed in figure 2.4. The integral corresponds to a summation of phasors that represent the exponentials in the complex plane. The head-to-tail arrangement of these phasors turns like a spiral as the point Q in figure 2.3 moves further away from point C (we assume circular symmetry). The chain of phasors spirals inwards due to the inclination factor in equation 2.8, that reduces contributions from wavelets that originate further away from point C. The value of the integral corresponds to the phasor pointing from the beginning to the end of the phasor-chain. This is indicated by the arrow in figure 2.4 for a circular obstacle. The point Z_0 is associated with a phasor at point C, while Z_j refers to the phasor at the edge of the circular obstacle. As Z_j moves along the spiral the magnitude of the arrow only decreases very slowly. This shows that the on-axis intensity closely corresponds to the intensity without the obstacle, which is represented by the phasor $\mathrm{Z}_0\mathrm{Z}_\infty$. This explains the existence of the on-axis bright-spot, called Poisson spot.

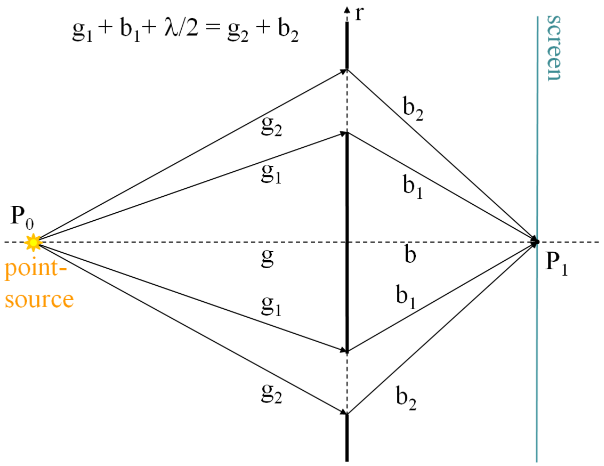

Figure 2.5: Fresnel zone. An annular aperture as indicated by the thick black line and with dimensions such that the equation g_2+b_2 = g_1 + b_1 + $\frac{\lambda}{2}$ holds almost doubles the field and quadruples the intensity at point P_1. This follows from the vibration curve in figure 2.4. The area of the annular aperture is referred to as a Fresnel zone. Blocking alternate Fresnel zones results in a bright beam focus, which can be achieved with a Fresnel zone-plate (see chapter 3).

The Poisson spot can be interpreted as a focus, and in fact a circular obstacle can be used to create an image of an extended source [85]. The Poisson spot from an extended (incoherent) source is not very bright (see next section), so that this is not very useful in practice. However, by using a simple trick one can amplify the Poisson spot. Again, we can use the vibration curve in figure 2.4 to visualize the trick. It is possible to maximize the outcome of the integration in equation 2.7, by removing all the phasors that have an upward (or downwards) component. They are the ones that make up the right (or left) half of the vibration curve. The result is that the halves of the vibration curve will be stacked on top of each other, yielding an increasingly longer resultant-phasor which corresponds to an increasingly larger on-axis intensity. In practice the removal of the phasors can be achieved by simply blocking the wave in the corresponding regions of the aperture-plane. Fresnel zone-plates, which are used (paper C and E) and fabricated (paper D) as part of this thesis, make use of precisely this idea to focus a wavefront. The areas in the aperture plane which correspond to phasors with either an upward or a downward component are referred to as Fresnel zones. An interpretation of this in terms of the source to screen path-length is given in figure 2.5.

2.2 Numerical simulation of the Poisson spot

Naive numerical calculation of the integral in equation 2.7 does not lead to accurate results, especially in the case of large Fresnel numbers. My master thesis [77] explains in detail how a satisfactory simulation can be implemented using the method described by Dauger [19]. Therefore, I just briefly summarize the main points here.

If the general aperture in the plane S is binary (i.e. either completely transparent or completely opaque) the field at point P_1 can be expressed in polar coordinates (ρ, θ) of the plane S to be proportional to [19]

$$U(P_1) \propto \int_0^{2\pi} \int_0^{\infty} g(r,\theta) e^{\frac{\mathbf{i}\pi\rho^2}{\lambda}\left(\frac{1}{g}+\frac{1}{b}\right)} \rho d\rho d\theta \tag{2.11}$$

where $g(r,\theta)$ is the aperture function and equals to 1 for transparent and 0 for opaque regions of the aperture. Solving the integral numerically using the trapezoidal rule or Simpson's rule is not efficient and is particularly numerically unstable for configurations with large Fresnel number. This is because the phasor fluctuates on an increasingly small scale for such configurations. However, one can express the ρ-integral for each particular angle θ as the following sum $R(\theta)$ over transparent sections $[s_j, t_j]$ along the ray which has azimuth angle θ. The ray originates at the intersection of the plane S with the line $\mathrm{P}_0\mathrm{P}_1$. P_1 is no longer necessarily on the optical axis since we want to calculate the intensity on the screen also at some distance from the optical axis.

$$R(\theta) \propto \sum_j e^{\pi \mathbf{i} t_j^2/2} - e^{\pi \mathbf{i} s_j^2/2} \tag{2.12}$$

The transparent sections are easy to calculate for a circular disc, since we only need to calculate the intersections of the ray with a circle which results in a quadratic equation. For transparent section that reach to infinity it is important to assign a value to the undefined object $e^{i\infty}$. This contribution can be set to 0 in the integral because the inclination factor will cancel any contribution from an edge at infinity [19]. The image in figure 2.1 was calculated using an implementation of this method.

2.2.1 Lateral distribution of the Poisson spot

If only the central part of the diffraction image is of interest as opposed to the whole shadow one can approximate the lateral intensity-distribution of the Poisson spot with a squared zeroth-Bessel-function of the first kind (J_0)[41]. For a source at infinity one can write for the intensity on the screen

$$I(P_1, r) \propto J_0^2\left(\frac{\pi r d}{\lambda b}\right) \tag{2.13}$$

where r is the distance of the point P_1 on the screen from the optical axis. d is the diameter of the circular object. b is the distance between the object and the screen. λ is the de-Broglie wavelength. The lateral intensity distribution calculated with this formula is shown in figure 2.6 together with a numerical calculation of the integral.

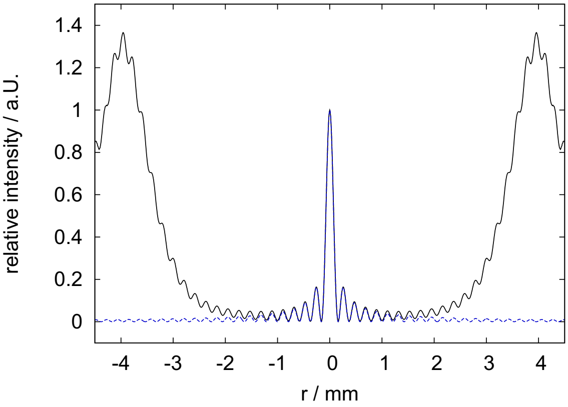

Figure 2.6: This graph shows the lateral intensity distribution of the image in figure 2.1. For the calculation I used the following parameters: λ=633nm (wavelength of a red helium-neon laser), g=b=1m, d=3mm. The image is 1000x1000 pixels in extend and the intensity of each pixel was calculated using 1009 angular steps. The dashed (blue) curve was calculated with equation 2.13

2.2.2 Spatially incoherent sources

The integral in equation 2.7 and the approximation in the previous paragraph represent the field at the screen from a point source. In the experiment the source-width was determined by the 50-µm-diameter skimmer. This is a very bad approximation of a point source. To compare the experimental data to theory it is necessary to convolute the source with the calculated point-source diffraction-image. Furthermore, the detector has a finite size which will also contribute to blurring the recorded image. In the model used in Paper A the source convolution is done by averaging the diffraction image from randomly displaced source-points. The source points are uniformly distributed within the 50-µm-diameter source. The diffraction images from the displaced source points are deduced by shifting the original diffraction image by a distance given by the geometrical magnification:

$$\begin{aligned} x_{image} &= x_{source} * \frac{g}{g+b} \\ y_{image} &= y_{source} * \frac{g}{g+b} \end{aligned} \tag{2.14}$$

Here (x_{source},y_{source}) and (x_{image},y_{image}) refer to the coordinates of the source and image points, respectively, in the corresponding planes orthogonal to the optical axis. This displacement of the diffraction pattern in the image plane is also the reason for why the Poisson spot from an extended, incoherent source is not as intense as the unobstructed wave. The sum of the diffraction images only makes the Poisson spot wider but not more intense, while for the unobstructed wave the full intensities are added on top of each other. So each summand from a displaced source point reduces the intensity of the Poisson spot with respect to the unobstructed wave.

Just as in the case of a lens the extended-source Poisson-spot is demagnified if $g > b$ and is larger than the source if $g < b$. For large distances from the optical axis it would not just be the position of the diffraction image that changes but it would also be distorted. This is because the circular disc will have an elliptical cross-section when viewed from such an off-axis source-point. However, since in the Fresnel approximation the source is very far from the circular object, this effect can be safely neglected. This also explains why in the Poisson-spot experiment when the spot is used to create an image from an extended source, the use of a circular disc or a sphere leads to approximately the same diffraction image.

The effect of the finite detector-size is simulated by a 2-d summation of the 2-d diffraction-image that resulted from the previous step. For each point in the image plane all the diffraction-image points within the circular neighborhood represented by the 11-µm detector-aperture are summed and appropriately normalized.

2.2.3 Edge corrugation

The Poisson spot can be understood as the positive interference of the Fresnel zone that is adjacent to the outer edge of the circular obstacle. With this kept in mind it comes as no surprise that corrugation of the outer edge of the circular object reduces the intensity of the Poisson spot. The width of the adjacent zone can be derived from the zone-plate formula (equation 3.7) and is given by

$$\Delta r \sim \sqrt{r^2 + \lambda \frac{gb}{g+b}} - r \tag{2.15}$$

where r is the radius of the circular obstacle. g and b are the source and image distances as before. If the amplitude of the corrugation is similar to the width of the adjacent Fresnel zone it can cancel the positive interference on the optical axis. Since the Fresnel zones become thinner as the screen moves closer to the circular obstacle, the finite corrugation of the circular obstacle eventually dampens the Poisson spot as one moves toward it. This is visible in the data presented in paper A.

To simulate the effect of edge corrugation I have varied the radius of the circular disc using a sinusoidal function as given in the following equation:

$$f_{corr}(\zeta) = C * \sin^4(\frac{2\pi}{\tau}\zeta) \tag{2.16}$$

where C is the amplitude of the corrugation, τ is the length of a period and ζ the position along the circumference of the disc. In the simulation for paper A I set $\tau = 0.83\mu\text{m}$. A smaller period would have been closer to the actual edge corrugation, but harder to resolve in the angular integration steps of the simulation. The 4^{th} power sine better represents the actual observed edge corrugation. In the simulation 10^4 points along the corrugated circumference are precomputed for efficiency. The point that fits best to the intersection of the ray with the circumference is then looked up in the pre-computed array, which significantly speeds up the calculation.

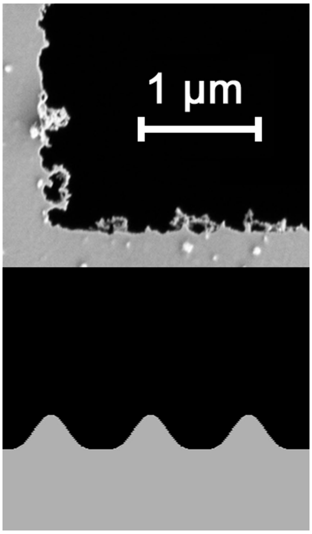

Figure 2.7: The image on the top shows a scanning-electron micrograph of the edge of the silicon-nitride disc used in the experiments of paper A. Below is a graphic of the edge corrugation that was used in the simulation (same scale). The correspondence is not ideal, but the shape in the simulation proved a good compromise between efficiency of the simulation and representing real edge-corrugation. Note also that the SEM image shows a region of the edge with minimal corrugation.

2.2.4 Wall interaction in the wave-picture

In paper B I extended the simulation to include interaction of the matter-waves with the circular object. Neutral atoms and molecules that pass close by a material wall are attracted to it due to dispersion forces, which represent an interaction between the atomic or molecular dipoles and the material wall. The dispersion forces between atom and surface at close range are generally referred to as van der Waals (vdW) forces [64]. While van der Waals deduced the existence of such an interaction potential between neutral atoms from deviations from the ideal gas law, it was J. E. Lennard-Jones [58] who determined that the interaction can be described by a potential of the form

$$V(z) = -\frac{C_3}{z^3} \tag{2.17}$$

where C_3 is a material-dependent constant and z is the distance between the atom and the surface. This potential is accurate as long as the atom or molecule is not so close to the surface that the microscopic surface structure becomes important. In general this is the case if $r \geq\sim 1$ nm [39]. At greater distances retardation modifies the potential to be $\propto r^{-4}$, which is then referred to as the Casimir-Polder potential [16]. The deviation is a direct result of the quantum fluctuations of the electro-magnetic field. The effect is negligible if the distance r is small compared to the wavelength of the most probable electronic transition within the atom or molecule [92].

For a wave the potential induces a phase shift which is approximately given by [71]

$$\phi(z) = -\frac{V(z)d}{\hbar v} \tag{2.18}$$

where d is the length along which the wave is affected by the potential, v is the beam velocity and $\hbar$ is the reduced Planck constant. As mentioned in paper B this vdW-phase was included in the model by taking it into account in the Fresnel-Huyghens principle:

$$U(P_1) = -\frac{\mathbf{i}}{\lambda}\frac{Ae^{\mathbf{i}k(g+b)}}{gb}\int\int f(r,\theta)e^{\frac{\mathbf{i}\pi}{\lambda}(\frac{1}{g}+\frac{1}{b})r^2+\mathbf{i}\phi(z(r))}rdrd\theta \tag{2.19}$$

Unfortunately the distance z from the surface was falsely identified with r the distance along the ray in the line integration of the algorithm (which is performed for each angle θ in the aperture plane). However, the simulation did calculate the distance $z(r)$ correctly in the numerical implementation of the line integral. There the integral was calculated using the trapezoidal rule and was tested to give the correct results for $C_3 = 0$.

2.2.5 Wall interaction in the particle-picture

Inconveniently, the classical interaction of a particle with the wall leads to a similar bright spot as in the wave-picture. Observation of the spot alone is therefore not a definite expression of the wave-nature of the beam-particle. The particles passing by the circular obstacle at a distance z are attracted to it by a force F corresponding to the vdW potential in equation 2.18:

$$F(z) = -\frac{dV}{dz} = -\frac{3C_3}{z^4} \tag{2.20}$$

For a perfectly circular obstacle and a particular distance $z = z_1$ from it, the particles will meet at a single spot on the optical axis in the obstacle's shadow. This leads to a theoretical divergence of the intensity on the optical axis in the particle picture. However, corrugation of the circular object's surface has the result that particles close to the edge are deflected onto trajectories that do not meet the optical axis. In paper B I found that the dependence of the resulting finite particle bright-spot on edge-corrugation is different than in the wave-picture. The easiest distinction between the two pictures would hence be to measure the total intensity of the Poisson spot from discs with varying amount of disc-edge roughness.

Finally it should be noted that the actual vdW potential close to the corrugated edge is not as simple as I have assumed in the model (see the restrictions mentioned in conjunction with equation 2.17). Dispersion forces are not additive, meaning that the forces between three atoms are not a simple addition of the forces between each pair [64]. In fact it is even possible for certain geometries to result in a repulsive dispersion potential [50]. However, I assume that the deviations from a simple $\propto 1/z^4$ are only important for a certain distance range from the corrugated edge, which will only lead to minor changes in the spot-intensity predicted by the model. In particular I do not expect more intensity in the particle bright-spot since it is unlikely that the force vectors are adjusted so as to lead to better focusing.

2.3 Experimental setup

The configuration of the experimental setup for the Poisson-spot experiment is described in paper A as well as my master thesis [77]. Further details on the supersonic-expansion apparatus that was also used in all the zone-plate focusing experiments can be found in the Master Theses by Apfolter [2] and Koch [54]. Therefore I only give a brief overview here. A schematic of the setup is shown in figure 2.8.

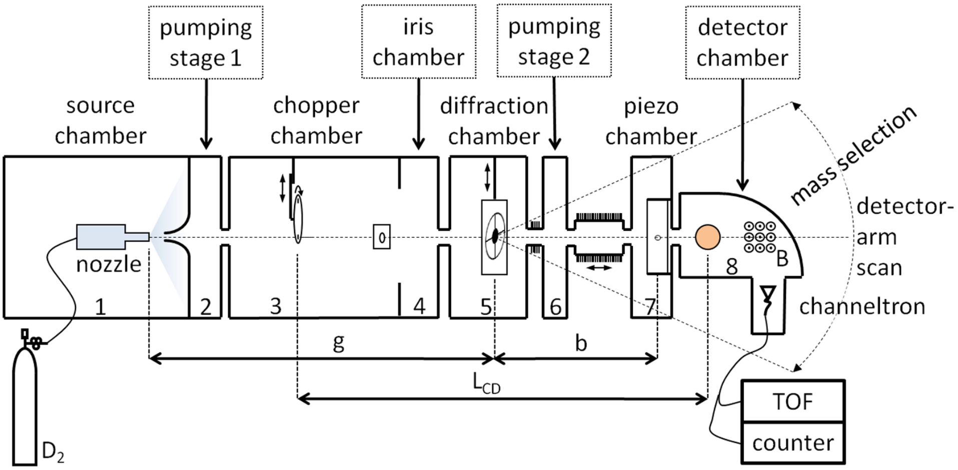

Figure 2.8: Schematic of the supersonic-expansion beam apparatus (Magie). For the Poisson-spot experiments the expansion gas was normal, molecular deuterium (D_2). The beam was collimated with a 50-µm-diameter glass skimmer and a 400-µm-diameter aperture. The chip with the suspended silicon-nitride disc was mounted in chamber 5 on a differentially pumped UHV manipulator. The intensity in the beam-shadow behind the disc was measured by stepping an 11-µm-diameter hole-aperture in the imaging plane using a piezo-table. The molecules passing through the aperture are ionized by electron-bombardment, then mass-selected in a magnetic sector and finally detected in a channeltron. The count-rate is recorded in a CAMAC system in conjunction with Labview software on a personal computer.

2.3.1 Ultra-high-vacuum system

Each of the eight vacuum-chambers of the apparatus is pumped with the combination of a turbo-molecular pump and a mechanical pre-vacuum pump which are 2-stage rotary-vane pumps, except for the diffraction chamber where the backing vacuum is established with an oil-free scroll pump. The pumping-speed for the source chamber is in addition increased by two roots pumps in series. The vacuum pressure in the chambers is monitored with a combination of Bayard-Alpert and Penning gauges. Pirani gauges are used to measure the pre-vacuum pressures between mechanical pump and turbo pump, which are usually about 10^{-2} mbar due to the long (up to 15m) prevacuum lines (the prevacuum pumps are located in a separate room to reduce apparatus vibration). Zeolith oil-traps are used to prevent the back-diffusion of oil from the non-oil-free mechanical pumps to the vacuum chambers. A list of the pumping speeds

	vacuum chamber	S_{tp} / l/s	S_{mp} m^3/h	p / mbar
1	source chamber	3200	65,500,250	$1x10^{-6}$ ($1x10^{-3}$)
2	pumping stage 1	380	16.5	$1x10^{-7}$ ($1x10^{-6}$)
3	chopper chamber	520	4.2	$1x10^{-8}$ ($1x10^{-7}$)
4	iris chamber	48		
5	diffraction chamber	520	5	$5x10^{-9}$
6	pumping stage 2	52	8.5	$1x10^{-9}$
7	piezo chamber	50,50	4.2,4.2	$5x10^{-7}$
8	detector chamber	520	8.5	$3x10^{-10}$

Table 2.1: Vacuum chambers and specification of the vacuum pumping-system of the molecular-beam apparatus called MaGiE (stands for 'Makroskopisch Gitter Experimente', German for 'macroscopic lattice experiments'. S_{tp} is the pumping speed of the turbo pump which is attached to the corresponding chamber and S_{mp} is the pumping speed of the pre-vacuum pumps. p refers to the vacuum pressures measured in the chambers. The pressures indicated in brackets indicate approximate pressures measured when a high pressure is applied to the nozzle.

and commonly achieved pressure for each chamber is given in table 2.1.

An electronic surveillance system monitors pre-vacuum pressures as well as cooling-water supply and turns the turbo pumps off if either of them is insufficient. High-voltage in-vacuum systems such as the detector, the quadrupole mass-spectrometer in the diffraction chamber or the piezo-table are only supplied with power if the pressure-gauges of the corresponding chambers read a pressure above a certain threshold. The pressure thresholds are set in the pressure-gauge controllers via the front-interface. The surveillance system also ensures sufficient vacuum pressures and cooling water for chopper operation(see section 2.3.4).

2.3.2 Supersonic-expansion source

The source of the beam is mounted on a manual micro-stage with 4 degrees of freedom in the box-shaped source chamber. This way the beam is aligned with the optical axis of the apparatus. In the source high pressure gas (1-200 bar) is expanded into the vacuum chamber via a 10-µm-diameter exchangeable platinum nozzle. The source-body is made from copper which is connected to a liquid-nitrogen cryostat via two approximately 15-mm-thick copper braids. A heating wire (supplied by company Thermocoax) is wound around the source-body and a Pt-100 resistance temperature-sensor is attached to the copper-source-body so that the temperature of the source can be controlled within the ranges 100-150 K and 300-350 K with a precision of about ±0.1 K. The actual temperature of the expanding gas may deviate due to local cooling or heating of the gas in the expansion (see paper E). The source pressure is measured with a Bourdon gauge (precision $\pm 1\%$). The source gas had a purity rating of 5.0 (normal D_2) or 6.0 (He). During beam production the background-pressure in the source chamber rises to about 1x10^{-3} mbar for p_0=200 bar and T_0=300 K. The beam enters the pumping stage 1 chamber via an exchangeable beam skimmer. For the Poisson-spot experiment and the microscopy experiments glass-micro-skimmers [10] were used, while for the imaging of the virtual source of a deuterium source in paper E a 400-µm-diameter nickel skimmer was used (supplied by company Beam Dynamics Inc.).

For the Poisson-spot experiment a beam pressure of p_0=10 bar and a nozzle temperature of T_0=101 K was used. At these source conditions condensation is still negligible (see paper E). At higher pressures the beam-signal counted at the detector through the 11-µm-diameter aperture first decreased sharply and then slowly increased again. This can be attributed to the condensation in the source which reduces its brightness, and therefore reduces the amount of particles that pass through a source-limiting skimmer. Incidentally, the prediction by the model in paper E indicates that the virtual source size is about the size of the skimmer for the source conditions of the Poisson-spot experiment. For higher pressures the virtual source-size would increase beyond the skimmer size and condensation additionally reduces the brightness of the source, which explains the intensity maximum found at p_0=10 bar.

2.3.3 Electron-bombardment detector

The beam is detected using an electron-bombardment detector [80]. A high-current electron-beam is emitted from a barium oxide cathode whose emission current is controlled by varying the heating current. For the Poisson-spot experiment an acceleration voltage of U_K=160 V was used and the emission current was set to I_{em} =10 mA. These increased settings were used to maximize the count-rate at the detector. The usual settings are I_{em} =4 mA and U_K=200 V. For the deuterium-expansion measurements in paper E the acceleration voltage was reduced to U_K=80 V to reduce cluster fragmentation due to the electron-beam.

For the Poisson-spot experiment a small 11-µm-diameter aperture determined the entrance opening to the detector. This aperture is mounted on a piezo-table (range 80 µm by 80 µm with a resolution of 20 nm) inside the piezo chamber. This aperture also divides the chamber into two halves which are pumped by two separate pump combinations. This avoids an increase in the detector background especially when a large amount of beam signal reaches the piezo chamber and is blocked by a small aperture. Beside the piezo table the beam can also be scanned in the horizontal direction by rotating the whole detector arm (pumping stage 2, piezo chamber, detector chamber). The center of rotation is the center of the diffraction chamber in this case. The resolution of the steps depends on the position of the piezo-table aperture on the detector arm along the beam axis.

After ionization the ions are sent through a variable magnetic field for mass-selection. The transmission and resolution (m/δm) of the mass spectrometer are about 70 % and 25, respectively. The ions of a specific mass are then detected in a channeltron. The preamplified electric pulses are discriminated and transmitted to the CAMAC counting electronics via a 800 Mhz fibre-optic link. The beam signal is recorded on a personal computer using a Labview Program. The read-out from the CAMAC bus is achieved via a GPIB interface.

2.3.4 Time-of-flight setup

The energy-distribution of the beam can be measured using a time-of-flight setup. A chopper that is mounted on a vertical translation arm can be used to chop the beam into short beam pulses. The beam pulses are then detected in a time-resolved manner and integrated over many beam pulses. The broadening of the beam pulses reveals the speed distribution of the particles by also measuring the distance between chopper and detector. This distance was L_{CD}=(2010±10) mm for a detector position of b=(836±10) mm (Absolute position reading on detector arm L_D=580 mm). The chopper wheel has two slits with triangular shape, so that the slit width can be varied. In this thesis a slit width of 1.2 mm was used (chopper position: 1.020 inch, Chopper radius: 68.3 mm). The rotation speed was usually set to 275 Hz, lower than the maximum of 500 Hz since a comparatively thick chopper wheel was mounted and overheating of the chopper-motor had to be avoided. The finite size of the ionization-region artificially broadens the measured time-of-flight distributions. To deconvolute the width of the time-of-flight distribution it was assumed that the atoms or molecules are ionized over a length of 4.6 mm [80]. The analysis of time-of-flight spectra is discussed in detail in section 5.2.1.

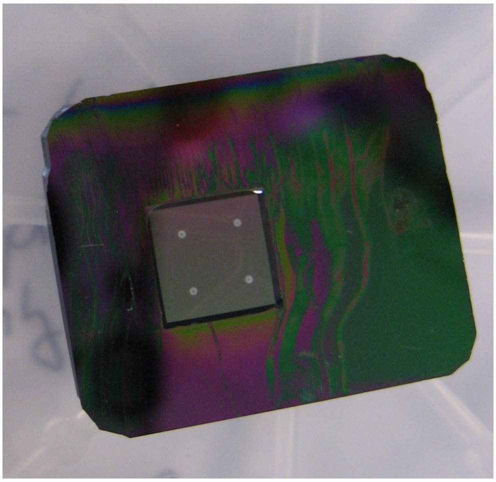

Figure 2.9: Silicon-nitride membrane-chip with four suspended circular discs.

2.3.5 Sample stage

The diffraction gratings and the Poisson-spot disc samples were mounted in the diffraction chamber on a stage with six degrees of freedom. The stage can be moved in the beam direction as well as orthogonal to it using a stepper motor (resolution 400 steps per mm). Access to the chamber is simplified via a ultra-high-vacuum o-ring-sealed door. The chip with the free-standing circular discs used for the Poisson-spot measurements is shown in figure 2.9.

2.4 Discussion

This section summarizes the results from papers A and B on the Poisson spot and gives an outlook towards possible experiments in the future.

The Poisson-spot experiment was carried out with a supersonic-expansion molecular-deuterium beam. The diffraction images measured at a varying distance behind the circular free-standing silicon-nitride disc fitted well with the predictions of a Fresnel-diffraction model. The model had to take into account edge-corrugation of the disc. The effects of van-der-Waals interactions were negligible in this experiment as was later confirmed by the model calculations in paper B.

The application of using the Poisson-spot experiment to demonstrate the wave-nature of large molecules was discussed in paper B and was also studied by Juffmann et al. [48]. The main result is that it is possible to clearly distinguish between wave and particle by comparing diffraction patterns from circular discs with different amounts of edge-corrugation. Furthermore, the simulations in paper B show that it might be feasible to perform the Poisson-spot experiment with a larger molecule such as C_{70}, but also that the scaling to larger atomic masses is not favorable. We predicted a count rate of about 10^{-4} s^{-1} for a hypothetical Poisson-sot experiment with C_{70}.

Nevertheless, one interesting feature that remains in this respect is the independence of the on-axis interference condition on wavelength. Especially for large clusters, which it would be interesting to demonstrate the wave-nature of, it is inefficient to select clusters of a particular de-Broglie wavelength. This is because the corresponding sources generally produce a large spread in cluster size. One way to lessen the unfavorable scaling would be to do many Poisson-spot experiments in parallel. The blocking discs would have to be small (a few micron) in such experiments anyway, so that a large number of discs could be placed next to each other. It may be advantageous for the contrast to replace each disc with a zone-plate-type pattern that takes phase-shift from the van-der-Waals interaction into account. This would however increase the dependence on wavelength. Such an experiment would require a large number of well-collimated beam sources, each aligned with the diffraction disc, and also a large number of scanning apertures that have to be equally well aligned. The required nano-structured and highly-accurate arrays of pinhole apertures and discs could be fabricated with the methods described in section 4.4. A Poisson-spot experiment with large clusters is currently planned at the Karlsruhe Institute of Technology which will attempt to provide a cluster beam with sufficient spatial coherence by filtering the beam with long micro-tubes [36].

I have also attempted to observe a Poisson spot using helium gas instead of deuterium. Unfortunately this was not possible on the apparatus described in the previous section. This was mainly because of two reasons. The supersonic expansion of helium exhibits abnormal behavior, due to a change in the quantum-mechanical collision-cross-section [70]. It results in high speed ratios of the beam, but also expands the virtual source [78] and reduces its brightness [22]. For this reason the maximum amount of beam flux that could be transmitted through the 50-μm-diameter skimmer was limited. Furthermore, the second reason is that the ionization probability of helium in the electron-bombardment detector is a factor of about 3 less than that of D_2.

Finally, we suggest in paper B that the Poisson-spot experiment could be used to study the Casimir-polder potential between molecules and different materials. By fabricating circular free-standing discs with suitable edge-corrugation it is possible to cancel the effect from pure diffraction, so that a bright-spot signal would be a direct result of the phase-shift associated with the Casimir-polder potential. A similar approach is planned in the field of astronomy from space. There a large disc at large distance is used to block the light from distant stars to be able to detect the much fainter light from any near-by planets [15]. One problem with this type of approach however would be the non-trivial form of the potential from a corrugated edge.

Chapter 3

Neutral helium microscopy (Paper C)

Microscopy techniques are important tools in numerous scientific fields and generally have a large impact on scientific progress. For example the scanning tunneling microscope [7] or the atomic-force microscope [8] have opened whole new areas of scientific studies of surfaces at the atomic level. The scanning electron-microscope [52] increased imaging resolution compared to the optical microscope by a factor of almost 1000. Even the diffraction barrier to resolution of the optical microscope has been overcome in stimulated-emission-depletion (STED) microscopy [51]. The impact on fields like biology cannot be overstated. Most of these microscopy techniques are readily available at most scientific institutions which is a clear sign of their importance.

In paper C we describe a relatively new microscopy technique that aims at using a ground-state-helium supersonic-expansion beam [70] as imaging probe by focusing it with a Fresnel zone-plate. A general schematic of this type of microscope is shown in figure 3.1. So far only transmission-microscopy images, i.e. with the detector behind the sample, have been recorded [53]. The paper presents the highest resolution transmission images so far, where the sample was a carbon film with 2-µm-diameter holes. The paper also demonstrates the focusing of deuterium molecules down to a focus of width 15.2±0.5 µm. This shows that the technique can be extended to other gases like molecular hydrogen or molecular oxygen.

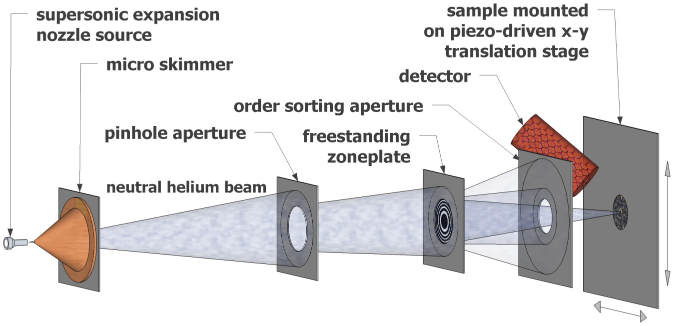

Figure 3.1: Neutral-helium microscopy-setup.

Neutral atomic or molecular beams can be focused in a number of ways. For example standing light-waves have been used to focus metastable helium atoms in one dimension [83] and two-dimensional periodic patterns have been created with a beam of chromium atoms [11]. This type of focusing is however not particularly suited to microscopy since the numerical aperture of the 'light-lenses' is limited by the wavelength of the laser. Another way to focus neutral matter-waves is to diffract them off an electro-statically deformed ultra-flat single-crystal surface[45] (using the zeroth order specular peak). This technique has been used to focus supersonic expansion beams of helium [45] to a focus of about 25 µm [31].

Fresnel zone-plates can in general focus any type of wave. They can focus light and are currently being considered as large objective lenses for space telescopes [56, 91], mainly because zone-plates can be patterned on thin and light plates or foils and are thus much cheaper to transport into space. They are used in ultra-high-resolution soft-X-ray microscopes which achieve a resolution of about 15 nm [74]. Furthermore, zone plates have been used to focus beams of neutrons [49], atoms [14, 23] and molecules as we show in paper C.

The ground-state helium beam we use here has been focused down to a minimum of about 600 nm [26]. The minimal possible focus width with current techniques is estimated to about 300 nm for a 200-µm-diameter zone-plate in paper C. This limit could be overcome by combining the zone-plate with a second type of lens that has an opposite dependence of the focal-length on the wavelength, as has been proposed for X-rays [93]. This lens could be implemented by tuning particle-wall interaction (van-der-Waals potential) or introducing electrostatic (quadrupole) or magnetic (hexapole) fields [18].

Beside focusing of the beam one major technical hurdle remains on the way to building a neutral-helium microscope. The detection of ground-state helium with electron-bombardment detectors is very inefficient. The state-of-the art detector in our lab [80] has an efficiency of about $2\text{x}10^{-6}$. One candidate detector which promises to be more efficient uses sharp tips to create a strong electric field that ionizes atoms and molecules (field-ionization) [24, 69, 72, 79]. A problem with field-ionization detectors is that they ionize particles only in a small ionization volume, which equally results in low signals. This could be solved by arranging the tips, for example carbon nanotubes, in two-dimensional arrays [94]. If a voltage is applied to each tip in sequence the array could be also used to create an image without the need to move the sample. In this case the sample would be exposed to the helium beam as a whole and the imaging zone-plate would create an image in the detector plane.

The advantages of a neutral-helium microscope stem from the neutrality and low energy (about 50 meV) of the supersonic-expansion helium beam. The helium atoms have so low energy that they do not penetrate into the bulk and therefore exclusively probe the top-most monolayer. Furthermore, the low energy of the beam means that the sample is not altered in any way, as for example an electron-beam in a scanning-electron microscope (SEM) would. The neutrality of the beam is an advantage because the sample does not charge up, which causes image distortion in an SEM. Also conductors and insulators can be imaged alike without the need of a conduction-coating. These properties make the neutral-helium microscope ideally suited to metrology applications and imaging of sensitive or fragile samples. The contrast in a reflection neutral-helium microscope would be mostly due to surface topology [60]. By using an image-probe with a permanent magnetic moment, as is the case for example with molecular oxygen, I would expect the microscope to offer magnetic contrast in addition.

A further application of focused molecular beams that is discussed in paper C is the study of molecular diffusion properties of porous or permeable materials. The focused beam can be stepped across a thin sample, as the molecules are detected on the other side. Time-resolved measurements would allow the measurement of diffusion constants and rate of physisorption, which are both very important parameters in the search for efficient carbon or hydrogen storage materials.

This chapter will be restricted to a short background on Fresnel zone-plates (section 3.1), followed by a brief note on the experimental setup. In the final section the results from the paper are discussed.

3.1 Fresnel zone-plates

In this section I give a brief summary of the theory of Fresnel zone-plates (see also references [44, 62, 75]) and how they are used in neutral-helium microscopy. In section 2.1.2 I have already defined the notion of a Fresnel zone. A Fresnel zone-plate only transmits through those Fresnel zones which positively interfere at point P_1. The situation is depicted in figure 3.2.

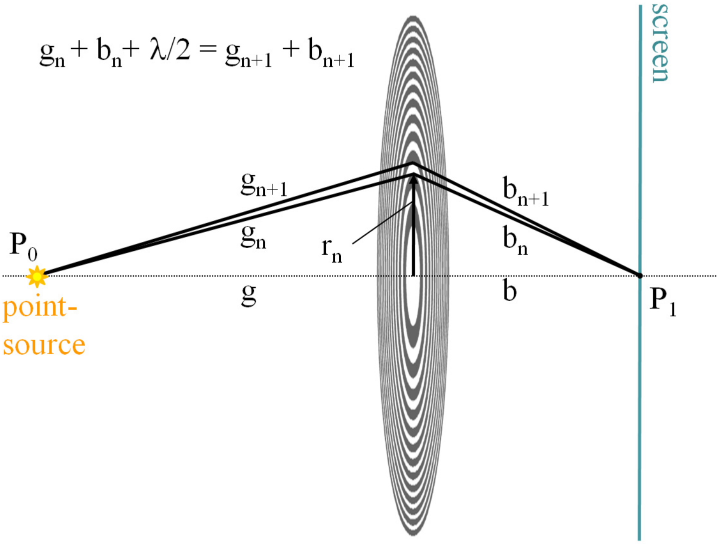

Figure 3.2: Notation for zone-plate construction equation 3.7. Odd Fresnel-zones are opaque and even Fresnel-zones are transparent (or vice-versa). r_n corresponds to the outer radius of the nth Fresnel zone (let g=g_0 and b=b_0). (after Rehbein [75])

3.1.1 Zone-plate construction equation

An expression for the radii r_n can be derived from simple geometric arguments by requiring that the path difference for waves that pass close to the edges of a Fresnel zone differ by half the wavelength:

$$g_{n+1} + b_{n+1} = g_n + b_n + \frac{\lambda}{2} \tag{3.1}$$

Expanding this recursive definition and using Pythagoras to express g_n and b_n in terms of r_n we can write instead

$$\sqrt{g^2 + r_n^2} + \sqrt{b^2 + r_n^2} = g_n + b_n + \frac{n\lambda}{2} \tag{3.2}$$

The equation can be solved exactly for r_n [62]:

$$r_n^2 = \frac{n\lambda(g+b)gb + \frac{1}{4}(n\lambda)^2(3gb + g^2 + b^2) + \frac{1}{8}(n\lambda)^3(g+b) + \frac{1}{64}(n\lambda)^4}{(g+b+\frac{1}{2}n\lambda)^2} \tag{3.3}$$

We can simplify this result by assuming that $n\lambda \ll (g+b)$ and thus terms of order two and more in $(n\lambda)$ can be neglected:

$$r_n^2 = \frac{n\lambda gb}{(g+b)} \tag{3.4}$$

For zone-plates that fit the experimental conditions of the helium-expansion apparatus (g=1500 mm,b=700 mm and λ=50 pm for a room-temperature-nozzle beam) this approximation is more than sufficient. Even for the radius r_{50000}, which corresponds to a zone-plate diameter of about 1mm, the error is only about 0.3nm.

3.1.2 Focal length of a zone plate

Consider a zone plate with N zones and r_N is the radius of the zone plate. If N is large, at least 100 [62], the focusing properties of the zone plate can be described in analogy to that of a thin refractive lens. Therefore we can associate a focal length f with the zone plate, which is defined by

$$\frac{1}{f} = \frac{1}{g} + \frac{1}{b} = \frac{N\lambda}{r_N^2} \tag{3.5}$$

In analogy to the thin lens the zone plate creates an image that is magnified by the factor

$$M = \frac{b}{g} \tag{3.6}$$

Using the focal length we can reformulate the construction equation 3.4 as follows.

$$r_n^2 = n\lambda f \tag{3.7}$$

The width of the outermost zone of a zone plate with sufficiently large N is given by

$$dr_N = \frac{\lambda f}{2r_N} \tag{3.8}$$

An amplitude zone-plate as we have described it here only consists of completely transparent or completely opaque zones. In this case the zone plate possesses many focal spots which correspond to the different diffraction orders in analogy to a linear grating. The m^{th} diffraction order is defined by adapting the positive interference condition in equation 3.1 to

$$g_{n+1} + b_{n+1} = g_n + b_n + \frac{m\lambda}{2} \tag{3.9}$$

The zone-plate construction equation thus becomes

$$r_n^2 = m\, n\lambda f_m \tag{3.10}$$

where $f_m = \frac{1}{m} f_1$ and f_1 is the focal length f defined in equation 3.5. This means that for each focal spot there is another one closer to the zoneplate. m can also be a negative integer, which results in divergent diffraction-orders with virtual focal points on the side of the zone plate facing the source. For an illustration see figure 3.3. The total intensity transmitted into specific diffraction orders diminishes with increasing absolute m, as is explained in the following section.

3.1.3 Diffraction efficiency

The diffraction efficiency of a particular diffraction order is defined as the ratio between the total intensity that is incident on the zone plate and the total intensity transmitted into that diffraction order. For the mth diffraction order it is give by [75]

$$\eta_m = \left(\frac{sin[\frac{a}{d} m\pi]}{m\pi}\right)^2 \tag{3.11}$$

where a is the width of a transparent zone and d is the width of a zone pair consisting of a transparent and an opaque zone. Here we will refer to the ratio a/d as the opening ratio of

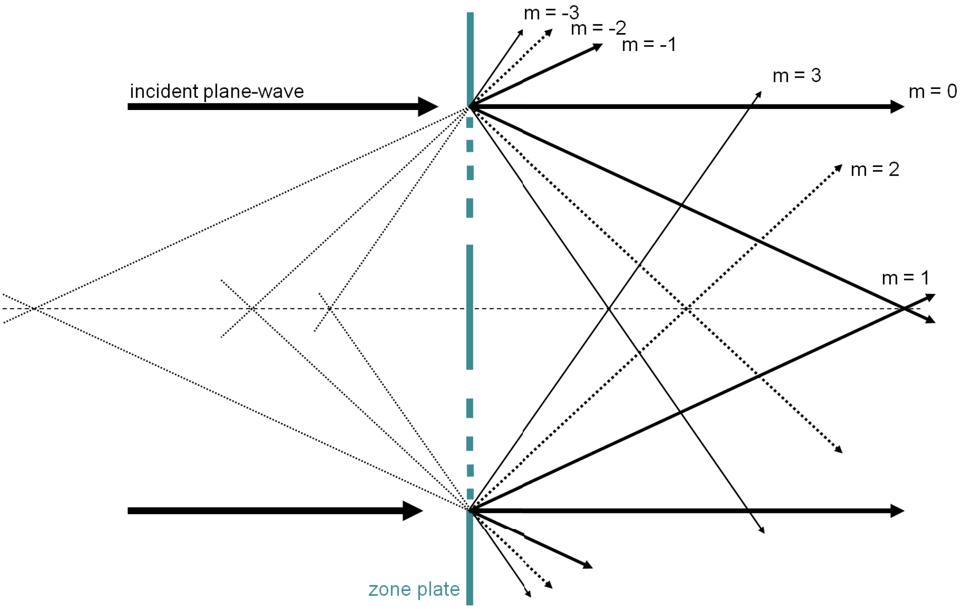

Figure 3.3: Focal points of an amplitude Fresnel-zone-plate with 1:1 ratio between blocking and open zones. The thickness of the arrows indicate diffraction efficiencies. 50 % of the total incident intensity is transmitted into the 0^{th} diffraction order. The $+1^{st}$ and -1^{st} take up about 10.1 % each. The even diffraction orders correspond to perfect destructive intereference, and therefore do not receive any flux. The $+3^{st}$ and -3^{st} receive about 1.1 % each. (after Rehbein [75])

the zone plate. The equation implies that the 0^{th} diffraction order, which corresponds to the beam passing through the zone plate without any deflection, receives 25 % of the incident total intensity for an opening ratio of 0.5 (then 50 % are blocked). In this case the $+1^{st}$ and -1^{st} take up about 10.1 % each, which is the maximum possible for the first diffraction order of an amplitude zone-plate. Hence, an opening ratio of 0.5 is ideal, since we intend on using the first diffraction order. No intensity is transmitted into the even diffraction orders, and only about 1.1 % can be found at the third order spots.

A zone plate that is designed for use with the third diffraction order could also have an opening ratio of 1/6 or 5/6. For these opening ratios the transmitted total intensity into the third order is equal about 1.1 % as in the case above. The intensity of the third-order focal spot is much more dependent on an exact value of the opening ratio. If the opening ratio is 0.6 instead of the intended 0.5 the first-order efficiency drops to 9.2 % which is a reduction of 20 %. At the same time the third-efficiency drops to 0.4 %, which is a reduction by more than 50 %. Therefore the observation of the higher diffraction orders can be used to determine how precise the zone-plate was patterned, which could be useful for testing fabricated zone plates in the future (see section 4.4.

The size of a zone plate is usually limited by the smallest outermost zone that can still be manufactured. However, there is a trick that allows an increase in the total amount of intensity captured by a zone plate. It is possible to extend a zone plate beyond the minimal zone-width radius with the wider zones of a zone plate whose third-order focus coincides with the first-order focus (composite zone-plate) [62].

3.1.4 Resolution of zone plates

The distance δ between two incoherent source points that can be resolved by a zone plate is approximately given by the width of its outermost zone [75]:

$$\delta = 1.22\frac{dr_n}{m} \tag{3.12}$$

Note that the resolution increases for higher diffraction orders. Nevertheless, equation 3.12 only applies to monochromatic illumination of the zone plate. For poly-chromatic sources such as the supersonic-expansion beam the resolution is determined by its wavelength distribution, since the focal length is indirectly proportional to wavelength (chromatic aberration). In paper C I show that the width of the first-order focus is given by [62]

$$w = \frac{r_N}{\lambda/\Delta\lambda} = 2\sqrt{\ln(2)} * \frac{r_N}{S} \tag{3.13}$$

where S is the speed ratio of the beam given by $S = 2\sqrt{\ln(2)}\frac{\lambda}{\Delta\lambda}$. That this equation applies quite well in the case of a helium supersonic-expansion beam can be seen in reference [53].

3.1.5 Order-sorting aperture and central block

The inner-most zones are blocked or not patterned at all in the zone plates discussed here. The reason for this is that the total intensity in the zeroth order is about 5 times larger than in the first order. In order to improve contrast the blurring zeroth order most be removed. This can be achieved by blocking the innermost zones of the zone plate and including an order-sorting aperture (OSA) in the beam path behind the zone plate (see figure 3.1. This way the contribution from the zeroth and the negative diffraction orders can be blocked completely from reaching the imaging plane. Simple geometry dictates that for a given distance of the OSA behind the zone plate b_{OSA} the radius of the OSA r_{OSA} must be in the range:

$$r_N\frac{b - b_{OSA}}{b} < r_{OSA} < r_{stop}\frac{g + b_{OSA}}{b} \tag{3.14}$$

where r_{stop} is the radius of the central blocking disc of the zone plate. The OSA must be at least a certain distance behind the zone plate. This is where the zeroth and the first diffraction order separate:

$$b_{OSA} > \frac{r_{stop}b + r_N g}{gb(r_N - r_{stop})} \tag{3.15}$$

The central blocking disc reduces diffraction efficiency and increases chromatic aberration [62]. Note that the simple geometric model for the chromatic aberration (i.e. equation 3.13 and figure 5 in paper C) does not take into account the effect of the central blocking disc. This is resolved in the focusing model used in paper E. Finally, note that the OSA should be as close as possible to the sample. Otherwise diffraction from the OSA might increase the focal width.

3.2 Experimental setup

The specific experimental setup both for measuring the neutral-helium transmission-microscopy image and the deuterium-beam focus are covered well in the paper. The apparatus was the same as used in the Poisson-spot experiment, so see section 2.3 for more information. Just briefly, for the imaging experiments the zone plate was mounted inside the diffraction chamber. Please refer to Koch's master thesis [54] for details on mounting fragile structures inside a vacuum chamber. The carbon foil sample was mounted on the piezo table inside the piezo-chamber after finding the focal plane of the zone plate. The latter was achieved by scanning a 25 μm by 3 mm slit across the focus and thus finding the optimal position of the detector along the optical axis of the apparatus. An order-sorting aperture with diameter 100 μm was mounted in the same plane as the sample. For each pixel in the top and bottom images of figure 3(b) in paper C, the detector-count was integrated for 21 seconds and 14 seconds, respectively.

To create a deuterium supersonic-expansion beam-focus the usual 50-liter helium gas-bottle (purity 6.0, supplied by Yara Praxair) was replaced with a 10-liter deuterium bottle (purity 5.0, normal D_2, supplied by Yara Praxair). The expansion of deuterium leads to a beam with a broader energy distribution compared with helium. The nozzle temperature had to be reduced from 320 K to 305 K to result in a beam of de-Broglie wavelength similar to the one for the helium beam. The actual wavelength of the beam was determined in time-of-flight experiments. For the scan of the focus a 25 μm by 3 mm slit was mounted on the piezo-table.

3.3 Discussion

The main result of paper C were two new neutral-helium microscopy transmission-images with the best resolution so far. The long integration times that were necessary to record the images show that the biggest difficulty with the technique at the moment is detector-inefficiency. This problem could be solved with new especially two-dimensional field-ionization detectors. The resolution in the images were limited by the chromatic aberration of the zone-plate. The calculations in the paper show that a minimal focus-width of about 300 nm could be achieved with currently available techniques. This limit could be overcome by combining the zone plates with electric quadrupole or magnetic hexapole lenses. Alternatively, mirror focusing which does not induce chromatic broadening could be used.

In addition a molecular-deuterium beam with an average beam energy of about 72 meV was focused to a spot of width 15.2±0.5 μm. This shows that beams from gases other than helium would benefit the most from correcting zone plates for chromatic aberration by combining them with other types of lenses. Molecular beam focusing like in this experiment could be used to study porous or permeable materials in a location-resolved manner and determine for example diffusion constants in time-resolved experiments. The deuterium beam was characterized in greater detail in paper E, where the beam focus and energy distribution was measured for a range of source conditions.

Chapter 4

Fabrication of free-standing zone-plates (Paper D)

In this chapter the background for Paper D is detailed. In addition unpublished results related to the Paper are presented. Paper D covers the fabrication and testing of Fresnel zone plates designed for neutral helium microscopy. The fabrication process, which I developed at MIT's NanoStructures Laboratory, is based on silicon wafers coated with 200-nm-thick non-stoichiometric (silicon-rich) silicon nitride (SiNx). The advantage of SiNx is its hardness and relatively high elastic modulus, which made it possible to create very sturdy membranes. The new process is based on work by Stefan Rehbein et al. [75], but differs in that the old zone plates were made using either silicon membranes or nickel.

The nickel zone plates made by Stefan Rehbein and coworkers were tested in Graz and were used to produce the first transmission helium-microscopy images [53]. During my master thesis I contributed to those experiments by developing a setup which reduced the thermal drifts due to lab-temperature fluctuations. This made it possible to record the finally published transmission-microscopy images with the highest possible resolution. As is detailed in Koch's master thesis [54], the nickel zone plates did not yield the expected transmission probably due to partially blocked outermost zones. The zone plates fabricated with the new process in silicon-nitride achieve a nearly ideal transmission. Only the zone plate patterned using multiple electron-beam lithography write-fields exhibited a reduction in first-order diffraction efficiency which we attributed to write-field-stitching errors.

The electron-beam lithography and fabrication aspects of the new zone plate process presented in Paper D are discussed in the first two sections of this chapter. The final section presents unpublished results on spatial-phase-locked electron-beam lithography (SPLEBL) [29, 43, 96] which attempts to avoid pattern-placement errors during electron-beam lithography. The idea is to use a high-precision reference grating (a so-called fiducial grid) fabricated using interference lithography to measure the deviation of the electron beam from the ideal placement. In particular I measured intra-writefield distortion for 200-µm writefields and fabricated zone plates whose pattern files were distorted to counter-act the measured distortion. Furthermore, I worked on fabricating zone plates using a segmented fiducial grid as a reference during patterning.

4.1 Electron-beam lithography

The Fresnel zone plates discussed in this thesis were fabricated using electron-beam lithography (EBL), where an electron-beam (e-beam) is used to expose an arbitrary pattern into a resist layer. This section covers details of the exposure strategy while the next section is concerned with the fabrication steps necessary to turn the exposed resist into a free-standing zone plate.

4.1.1 Introduction to electron-beam lithography and the Raith 150 system

There are three different types of EBL systems [43]. In a shaped-beam system the pattern is divided into simple shapes, which the electron-beam projects directly onto the substrate by means of apertures. Alternatively, the entire pattern can be formed using a mask which is then referred to as electron-projection lithography. Finally, the patterns can be formed by scanning the focused beam over the resist layer (Scanning EBL = SEBL). This is one of the more common techniques implemented in modern electron-beam lithography equipment, and is the approach of the Raith 150 EBL system[1]. The Raith 150 used for this project belongs to MIT's shared scanning-electron-beam-lithography facility (SEBL at RLE).

Next, one can distinguish between two different exposure strategies in SEBL. The first is referred to as 'raster-scan' and is mainly used in production. There the beam is scanned with high speed along one axis only, while the sample-stage is moved orthogonal to the beam movement. The pattern is formed by switching the beam on and off very quickly. The Raith 150 system in contrast follows a 'vector-scan' approach. This means that the sample-stage remains stationary during exposure and the e-beam 'fills' each contiguous area following an optimized path (left-to-right, boustrophedonic, or spiral).

A general schematic of a SEBL system is shown in figure 4.1. The main component is an electron-optical column with a source of electrons and various electro-static as well as magnetic lenses. It focuses an electron beam down to a very small spot (Raith 150: 2 nm) at a certain working distance from the final lens of the column. A set of deflection coils or plates make it possible to scan the beam-focus laterally across the substrate. The Raith 150 system uses a Zeiss Gemini[2] column which was designed for electron-microscopy [76]. The main advantage of using a microscopy column is its exceptionally small beam-focus which enables lithography at the highest possible resolution [95]. The high imaging quality allows the system to second as a tool for examination of fabricated nano-structures. The main disadvantages compared to other electron-beam lithography systems on the other hand are throughput and accuracy. The magnetic lenses of the Gemini column make fast and accurate beam placement difficult due to the simple fact that currents through the coil magnets cannot be changed infinitely fast. The result is that the system must wait a certain settling-time before the placement of the beam-focus is accurate, which then largely determines the time to perform an exposure as opposed to actual resist exposure. However, since throughput is not a big concern during

---

[1] Raith GmbH, 44263 Dortmund, Germany

[2] Gemini is a registered trademark of Carl Zeiss SMT Nano Technology System Division, 73447 Oberkochen, Germany

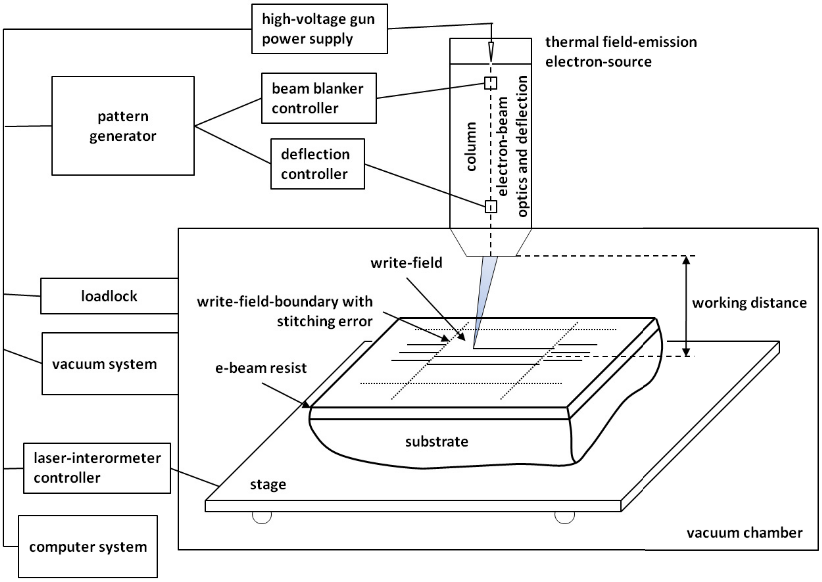

Figure 4.1: Schematic of a scanning electron-beam lithography system (after Zhang [96]).

process development or for tasks where only a small amount of patterned structures are required, such as our zoneplates, the Raith System is an excellent choice. If there is the need to structure larger areas the patterning steps can easily be transferred to a more expensive high-throughput system. Accuracy is important since the focusing-performance of the zone plate depends on the fidelity of the lithographic pattern. Section 4.1.2 looks at this point in greater detail.

The electron source crucially determines signal-to-noise ratio in imaging and available beam current in lithography applications. The Gemini column is equipped with a Schottky field-emission source, where a large electric field is applied to a sharp tungsten tip at elevated temperature (1800 K). The tungsten tip is coated with a zirconium-oxide electron-reservoir, which depletes after a certain amount of operation at which time the source needs to be replaced (approx. 2000 h). Other options for electron-beam sources include the cold field-emission gun and the lanthanum hexaboride (LaB_6) source. The latter is still used in electron-microscopes but is less bright than the Schottky field-emission source by a factor of 15 [84]. Cold field-emission from tungsten tips is brighter by a factor of two compared to its Schottky equivalent. However, the overall emission current is about 40 times less, which makes it less suitable to lithography applications.

The Raith 150 system has a maximal acceleration voltage of 30 kV [37]. Dedicated EBL-systems often use 100 kV and more. The main reason for this is that the higher electron energy makes it possible to expose thicker resist layers since the beam-focus has a larger focal depth and the energy is deposited more uniformly at different depths of the thick resist layer. This is not necessarily a major issue since, as the presented zone-plate process shows; One can use a thin e-beam-resist layer and transfer the pattern to a thicker secondary layer, which then serves as a resist for the pattern transfer to the intended material. It is clear however that the zone-plate-fabrication process could be optimized substantially on a dedicated EBL-system. For example one could write both support and zone-plate pattern at once (see section 4.1.3) into a thick resist layer and transfer the pattern directly to the silicon-nitride layer.

Beside the column there are a few more components that together form an EBL system. The pattern generator translates the electronic pattern-image into deflection signals that control the position of the e-beam focus on the substrate. The clock-rate at which the pattern generator functions limits the speed with which the beam-focus can be moved around. The Raith 150 system operates at a clock-rate of 10 Mhz. This is usually reduced to less than 5 Mhz due to the limit on the beam speed of 10 mm/s. Scanning the beam at faster speeds results in artifacts due to the magnetic nature of the electron-optics column. The pattern generator is usually however not the bottle-neck and was also not in this case. The pattern generator furthermore controls a fast electro-static beam-blanker, which serves to switch the beam off when the focus has to be moved across regions that are not to be exposed. The electronics of the pattern generator represent the surface of the substrate as discrete pixels which can be addressed individually by the beam. The address-space the pattern generator can handle is limited to a certain number of bits. For the Raith 150 system this is 16bit, and therefore the pixel of minimal size which can be addressed in a 100-µm square is 1.6 nm and in a 200-µm square it is 3.1 nm.

Since the beam can be deflected only to a certain small area on the substrate, it is important that the substrate can be moved laterally with the same precision as the beam movement, in order to make it possible to write large patterns. This is usually realized by a stage that is moved both by stepper motors and piezo-actuators. The stage position is measured using a laser interferometer. The Raith 150 system is equipped with a stage that can be moved with a precision of 2 nm.

Finally, all of the mentioned components as well as the vacuum system are controlled by a personal computer. The software on this computer can generate patterns or import them from certain file formats and translate them into a representation that is interpretable for the pattern generator. Furthermore, the software makes it possible to align the imaging field of the e-beam column with the substrate surface and calculate appropriate dwell-time based on the measured beam current and resist sensitivity. This project was performed on Raith's EBL software (version 4.0).

4.1.2 Pattern-placement in electron-beam lithography

The maximum area over which the e-beam can be deflected accurately is limited in most cases to an area of about 1 mm by 1 mm by the electron optics and deflection electronics. This area which can be addressed by the e-beam through deflection in a 'vector-scan' system is referred to as a write-field. Patterns which are larger than this maximal write-field size have to be stitched together by moving the substrate between exposures. Therefore, the substrate is usually mounted on a high-precision interferometric stage which allows placement of the substrate with a precision of as much as 0.3 nm [43]. As mentioned before, the Raith 150 system is equipped with a stage that achieves a precision of 2 nm. However, even with the substrate fixed with respect to the interferometer mirrors, the actual position of the e-beam focus depends on many variables. These thus influence accuracy (deviation from theoretical pattern), precision (deviation from accepted standard length) and repeatability (deviation of placement from one exposure to the next) of the exposures. The following list summarizes possible error sources that affect pattern placement in EBL systems [43]:

1) digital-analogue converter quantization
2) substrate charging
3) mechanical vibration
4) stray EM fields
5) interferometer quantization
6) deflection hysteresis
7) sympathetic beam/stage motion
8) thermal gradients and variations
9) field calibration
10) substrate mounting distortion
11) deflection non-linearity
12) electron-optics distortions
13) interferometer mirror errors
14) stage calibration

The sources listed in items 1-6 affect placement on a short time scale (10ms and less) and therefore mostly cause errors within a write-field (Intra-field distortion). In the 200-µm write-field used here these errors result in an uncertainty in placement of about 20 nm on the Raith 150 system (and even 100 nm close to the edges of the write-field - see section 4.4.3). Items 7-10 on the other hand occur on a time scale of the order of one second and more, and therefore are more likely to contribute to placement errors between separate write-fields (Inter-field distortion). The final four items are quasi-static and are thus reproduced in each write-field [43].

These various types of errors affect the performance patterned zone plates in different ways. If the zone-plate pattern is merely scaled by a constant factor, it is only the focal length of the zone plate that is affected. The radii in formula 3.7 are just multiplied by a constant factor, which can be counteracted by a change in the focal length.

Next, suppose that the calibration of one of the deflection coils is wrong by a certain factor, so that the zone plate turns out ellipsoidal instead of circular. The effect can be deduced from the experiments by Coulson and Becknell [17] who studied the Poisson spot from elliptical plates. They show that the focal spot transforms into the evolute of the geometrical shadow which is star-shaped for an ellipse. If one half-axis of the ellipse is twice the length of the other, the spot is washed out to a shape that is roughly the size of the geometrical shadow. For smaller deviations from circularity, one can expect an increase in the size of the focal spot of the zone plate, but the total intensity of the spot should not be affected.

If the errors cause the circles to be discontinuous, as in the case of a zone-plate stitched together from many write-fields, it is possible that the errors reduce the first-order diffraction efficiency (FODE) of the zone plate. The FODE is defined as the total intensity transmitted into the first diffraction order divided by the total intensity incident on the zone plate (see paper D). The FODE is also affected if the ratio between opaque and transparent zones is not equal to 0.5.

On a shorter time-scale the above error sources cause line-edge roughness. The effect of roughened grating bars can be deduced from the results in papers A and B. If the line-edge roughness amounts to a significant portion of the grating-bar spacing, it will result in a dampening of the FODE.

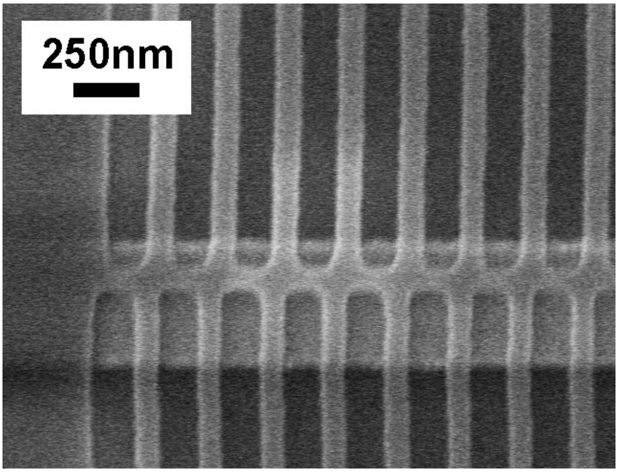

Figure 4.2: Stitching error at field-boundary. The horizontal bar is the nickel hard-mask for the support pattern (see next section) and the write-field boundary is parallel to it. The vertical lines should be uninterrupted. The stitching-error amounts to about 60 nm along the horizontal axis and 90 nm along the vertical axis. The top set of vertical lines was patterned about 90 minutes after the bottom set of lines. Hence, a large part of the error is most likely due to thermal drift.

Long time-scale errors significantly affect FODE, as can be seen from the measurement of FODE of the 4-write-field zone-plate (ZP_1). Beam drift in the Raith 150 system is as much as 300 nm per hour [37]. An SEM image of the worst stitching boundary in the ZP_1 pattern is shown in figure 4.2. From the image it is also clear that it is not line-edge roughness that leads to the reduced FODE.

Placement-errors can be reduced by providing a position and length-scale reference on the substrate. By re-aligning the write-field frequently or even continuously to this reference one can achieve a significant reduction in stitching errors. Some of the efforts to reduce placement errors in the zone-plate fabrication-process are described in section 4.4.

	support-bar exposure	zone-plate exposure
acceleration voltage	30 kV	30 kV
aperture diameter	20 µm	20 µm
typical exposure current	200 pA	200 pA
line dose	240 pAs/cm	300 pAs/cm - 525 pAs/cm
line step size	3.2 nm	3.2 nm
distance between paths	12 nm	9.6 nm
typical beam speed	8.4 mm/s	6.4 mm/s - 4.0 mm/s
typical dwell time	0.38 µs	0.48 µs - 0.84 µs
typical exposure times	15 min/write-field	30 min/write-field
working distance	12 mm	12 mm
write field size	200 µm	200 µm
magnification	320x	320x

Table 4.1: Parameters used to expose the support and zone plate patterns

4.1.3 Parameters for the zone plate exposures

The parameters used for the EBL exposures are summarized in table 4.1. The following paragraphs specify how each of the parameters was chosen and how their values influenced the fabrication process.

Support structure

The grating bars of the zone plate have to be free-standing in order to allow low-energy atoms and molecules to pass between them. To keep the circular grating bars of the zone plate in place it is therefore necessary to support them with radial bars. The required width of the support bars and the density of the support pattern was adopted from Stefan Rehbein [75], where it was assumed that 50-nm-wide grating-bars are stable if they are not longer than 1.5µm. In general the following criterion for the free-standing segments was used to create the support pattern:

$$\frac{length}{width} \leq 30 \tag{4.1}$$

Stefan Rehbein used 130-nm thick silicon membranes. Silicon-nitride is harder and has a higher elastic modulus than silicon, so that applying the same criterion should be more than sufficient for the eventually 150-nm-thick silicon-nitride membranes used here. The membranes are 150nm thick in the end because the final dry-etch step thins them down (see section 4.2.2).

Another similarity to Rehbein's process [75] is that the support pattern had to be written in a separate exposure. Examples of the zone-plate pattern and the support-bar pattern are shown in figure 4.3. Due to the rather large settling times the Raith system requires, it is advantageous to write long continuous lines as opposed to many interrupted line-segments. In principle it would be possible to expose the same resist-layer twice, with a development step in between.

This however makes it difficult to control grating-bar width, due to dose-additions from the proximity-effect.

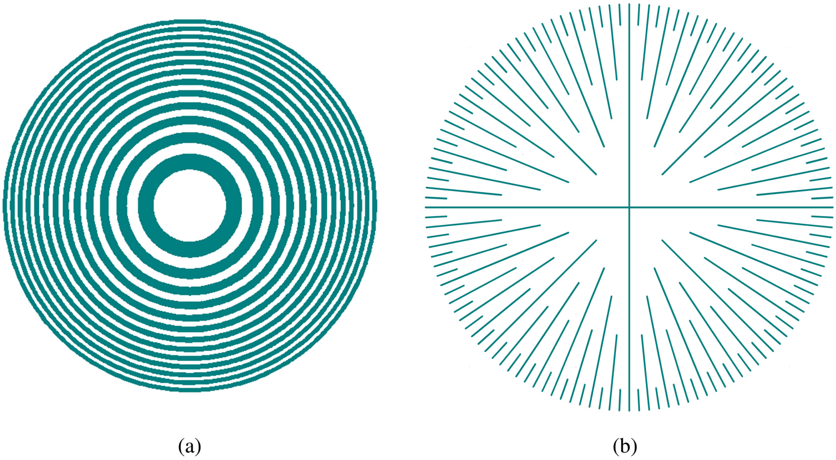
(a) (b)

Figure 4.3: Layout of a zone-pattern (a) and a support-bar pattern (b).

The proximity-effect refers to the fact that the sharp focus of the e-beam is surrounded by a low-intensity background focus with diameter of a few micrometer. This means that within the vicinity of every exposed pattern element, the resist surrounding it is also partially exposed. Therefore, for dense patterns the dose has to be reduced, to take into account the dose-addition from neighboring pattern elements.

Here, the support pattern is exposed first and transferred to a nickel hard-mask. The actual zone-plate pattern is exposed on top onto a tri-layer stack and transferred to the silicon-nitride membrane in three distinct dry-etch steps (see section 4.2).

Pattern design and input

The width of the zone-plate grating-bars and the support pattern are both defined by mathematical formulae. Creating either type of pattern in Raith's EBL pattern-editor would be very cumbersome. Furthermore, it was found that the final dose and actual beam path is not easily predictable in all types of area element (circle element or path element with a certain width). Therefore, it was deemed best to define the patterns as zero-width polygons, so that the beam would follow exactly the defined polygons. The pattern was created using a Matlab[3] script which outputs the polygons as an ASCII text file. The polygons are defined in Raith-specific syntax (`L [dose] [layer] [width]` followed by the vertex coordinates of the polygon).

In order to pattern uniform circles it was necessary to uniformly distribute the polygon start-vertices along the circular grating bar. This is because the dose deposited at the beginning of each polygon is slightly more than along the remaining beam path. Furthermore, it was

---

[3] MathWorks Inc., Natick, MA 01760-2098, United States

important to round the vertex coordinates to multiples of the line step-size, which was chosen as 3.2 nm for the zone-plate exposure. This is the minimum step-size for a 200-µm write-field. Without the manual rounding by the Matlab script, errors by the Raith-software would lead to unpredictable results.

The spacing between the polygons used to form lines of a certain width was chosen to be 9.6 nm for the zone-plate exposure, i.e. three times the line step-size. This means that the grating-bar widths and spacings could be only incremented by multiples of 9.6 nm. To fine-tune grating-bar width and spacing, the Matlab script added up to 75 % additional dose, leading to an increase in line-width. This part of the algorithm was optimized using a number of dose-matrix test-exposures.

A slightly larger line step-size and line-spacing was used for the support exposure to decrease exposure times.

E-beam energy and current

Both support and zone-plate exposure were performed with 30 keV beam-energy. For the support exposure this was important, since at lower beam energies it was not possible to see the edges of the silicon-nitride membrane through the resist-layer, so that the pattern could not be centered on the membrane. Similarly, it was important for the exposure of the zone-plate pattern which had to be aligned with the existing hard-mask support-pattern. For this reason the support pattern included four alignment marks. With the 30 keV beam-energy it was possible to image these alignment marks even below the tri-layer coating, while they were invisible at 10 keV. At 10 keV the e-beam does not penetrate as deep into the sample. One alternative would have been to dry-etch through the tri-layer coating on top of the alignment marks, but the above choice of beam-energy made this rather tedious option redundant.

The beam-current had to be reduced by using the smaller 20-µm aperture (the 30-µm aperture is standard), in order to keep beam-speeds below the recommended 10 mm/s. The typical beam-current used in the exposures was 200 pA.

Dose

For reasons explained in section 4.2.2 all patterning steps were performed on 200-nm-thick membranes (i.e. after removal of the silicon underneath). This had the advantage that the width of the patterned grating-bars could be controlled more precisely, because the effective focus-width due to secondary and back-scattered electrons is smaller. In principle this should also positively affect the resolution of the patterns, although this was not confirmed here.

Writefield size

The zone-plate pattern is not particularly suited to the vector-scan method. If the zone plate is patterned in a single write-field the highest resolution is required towards the edges of the write-field. However, this is usually where resolution and pattern-placement is the worst.

layer type	aquaSAVE (Mitsubishi Rayon Co., Ltd.)
thickness	≈60 nm
spin speed	3500 rpm
hotplate bake	90 s @ 175°C
removal of conduction layer	rinse with DI water

Table 4.2: Parameters for conduction-layer.

Therefore, there is a trade-off between write-field size (to pattern larger zone-plates) and the minimal resolution at the edges of the write-field. The largest write-field in which one would still be able to pattern 50-nm-wide lines was determined to be the 200-µm write-field at a column magnification of 320x. To achieve the required resolution the working distance had to be increased to 12 mm from the standard 6 mm that would be used in conjunction with a 100-µm write-field. This is because a less precise set of beam-deflection electronics is used for a magnification of 320x at a working distance of 6 mm [65].

To pattern zone plates larger than 200 µm in diameter, it was necessary to stitch the pattern together using a number of write-fields. This was successful for only one zone plate (chip #9, membrane #5 - see table 4.10). The Raith-150 system had difficulties handling very large pattern files, causing it to run out of memory after a certain exposure time. This was solved by keeping each zone-plate quarter in a separate pattern file, in essence keeping the Raith-software from determining the stitching boundaries by itself.

Conduction layer

The silicon-nitride layer used here is silicon-rich (SiN_x) and was deposited using low-pressure chemical-vapor-deposition. The stress in the membrane layer is minimized by the non-stoichiometric composition of the layer. Stoichiometric silicon-nitride is a very good insulator, but the silicon-rich type has some residual conductivity. This was enough to successfully pattern on the membrane without a conduction layer. However, it was deemed possible that localized charging could distort the pattern, since the actual conductivity was unknown. Therefore it was decided to apply a spin-on conduction layer on top of the resist. The details of application and removal are given in table 4.2.

Resist

The electron-beam resist used in this project was poly(methyl meth-acrylate), in short PMMA. The e-beam alters PMMA during exposure by chain scission. The thus lighter polymers are dissolved faster in the developer which here was a mixture between the organic solvent Methyl isobutyl ketone (MIBK) and iso-propanol (IPA). It is thus a positive-tone resist, which means that exposed resist is removed in the development process. PMMA can also act as a negative-tone resist at a much higher dose, which can be useful for high-resolution lithography [25]. The polymers are cross-linked in that case instead of broken apart. In this thesis PMMA was solely used as a positive-tone resist.

	support-bar exposure	zone-plate exposure
resist type	PMMA	PMMA
thickness	120 nm	50 nm
spin speed	5000 rpm	3000 rpm
concentration	$\approx$1.8% in Anisole	1.5% in Anisole
molecular weight	950k	950k
hotplate bake	90 s @ 175°C	90 s @ 175°C
development solution	MIBK:IPA (1:2) at 21°C	MIBK:IPA (1:2) at 21°C
development time	90 s	90 s

Table 4.3: Parameters for resist-layer and development process.

The parameters for the resist layer and its development are given in table 4.3. The thickness of the PMMA layer used for the zone-plate exposure had to be reduced to 50 nm, since the outermost zones would not resolve entirely in the thicker 100 nm PMMA layer.

Another challenge was spin-coating the finished membrane chips. The vacuum usually holding the chips in place during spin-coating would rupture the membranes. This was solved by attaching the membrane chips on a four-inch prime-wafer using a cut-out piece from a gel-pak container[4]. The membrane chips would safely stick during the spin process and could be removed without breaking the membranes.

4.2 Zone plate fabrication process

This section describes the processes used to fabricate the free-standing zone-plates from the exposures discussed in the previous section. Most of the process steps were performed in a class-100 cleanroom at MIT's NanoStructures laboratory.

4.2.1 Introduction to planar fabrication

The history of the integrated circuit (IC) is an unprecedented success-story. ICs have transformed human every-day life in many different aspects such as for example communications (mobile phones or the Internet) and entertainment (mp3/mp4-players or TV-sets). The leading example of an IC is still the computer's central-processing unit (CPU). Following Moore's law [66] the number of transistors in CPUs still doubles approximately every two years. This progress has been and still is largely enabled by lithography and the planar fabrication methodology. The basic concept is shown in figure 4.4. A substrate, for example a silicon wafer, is coated with some material that is to become part of a certain device. A resist-layer is applied and exposed with a certain pattern. This can be achieved by exposing with some form of radiation (e.g. ultra-violet light) through a pre-manufactured mask as is shown, or using a mask-less exposure as in the case of SEBL. After developing away the exposed or unexposed resist, the

---

[4] Gel-Pak, Hayward, California 94544, United States

pattern can be transferred to the device-material layer in a number of different ways.

SEBL is used today mainly to fabricate the projection masks, which are then used to replicate device patterns in large scale production using UV lithography. The minimal feature-size used in large-scale production is about to be reduced to 22 nm this year and integration is starting to make use of the vertical dimension [47]. The radiation used to project the mask images onto the substrates is still a 192-nm wavelength excimer-laser, although shorter-wavelength (about 13nm) extreme-UV plasma-sources are already sold as part of pre-production tools by ASML [4].

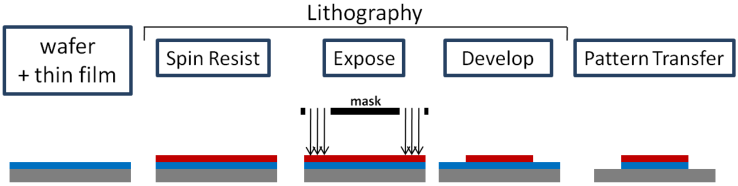

Figure 4.4: Planar fabrication.

4.2.2 Process details

Silicon-nitride membrane wet-etch

The raw substrate that was used for fabricating the zone plates was a silicon 100 wafer coated with 200-nm-thick low-stress silicon-nitride. The silicon-nitride layer was deposited in a low-pressure chemical-vapor deposition (LPCVD) step at MIT's Microsystems Technology Laboratory (MTL) using a gas-mixture of 10:1 SiH_2Cl_2:NH_3 at 780°C [81].

The first step was to pattern the backside of the nitride wafer using contact UV-lithography. The process steps and materials used are summarized in table 4.4. A positive resist (Shipley[5]) was exposed through a transparency mask (5080dpi from PageWorks[6]). After development the membrane-chip pattern was etched into the silicon-nitride layer in a dry-etch step with tetrafluoromethane (CF4). The silicon-nitride then served as a hard-mask in the potassium-hydroxide (KOH) wet-etch.

The wet-etch used to etch through the silicon wafer is a long process step (about 8 hours). For this reason it was decided that a large number of chips each with 9 membranes (see figure 4.6) should be produced first and the processing be done directly on the free membranes. The main disadvantage of this is that during all process steps care has to be taken so as to not break the membranes. It also has to be noted that spin coating does not result in perfectly uniform layers on such membrane chips. Also cleaving the silicon wafer into small chips often resulted in small parts of the under-etched silicon-nitride layer to break off and litter the chip surface.

The following advantages however seemed to outweigh these negative points. The proximity effect during e-beam exposures is less of a problem on thin membrane samples, as mentioned

---

[5] Marlborough, Massachusetts 01752, United States

[6] Cambridge, MA 02141, United States

resist	type spin speed thickness bake	Microposit S1813 60 s at 5000 rpm $\approx$ 1200 nm 120 s at 90°C
exposure	tool time	Tamarack Mercury lamp 20 s
development	solution time and temperature stopper solution stopping time	Microposit 351 rinse for 50 s at room-temperature de-ionized (DI) water rinse for 120 s
dry-etch	tool gas power pressure flow time	Plasmatherm 790 CF4 100 W 10 mtorr 15 sccm 10 min
wet-etch	solution time and temperature stop	20%(weight) KOH in DI-water 8 hours at 80°C rinse in DI-water

Table 4.4: Contact UV lithography to fabricate membrane chips

before. Another reason is that the wet-etch did not always work as expected due to unknown factors, so that it was more reliable and less time-consuming to perform the step for many chips in parallel and at the beginning of the fabrication procedure. In addition, aligning the transparency mask on the backside of the wafer with an existing pattern in silicon-nitride on the other side of the wafer would have been difficult with the tools at hand.

Nickel lift-off

After the support pattern for the zoneplate (see figure 4.3) was exposed into the PMMA-layer on top of the silicon-nitride membrane, a hard-mask was created by lifting off a 20-nm-thin nickel-layer. Nickel does not etch in the CF4 plasma that is used to etch silicon-nitride, and most importantly it forms a continuous layer on the PMMA and thin membrane. Chrome and titanium layers of similar thickness for example would tear up into small flakes, due to stress between the metal layer and the silicon-nitride layer. The nickel-layer was deposited using a Temescal[7] electron-beam evaporator.

A schematic of an electron-beam evaporator is shown in figure 4.7. A high-power e-beam is focused onto a material reservoir (filled with nickel in the case described here). The e-beam melts and evaporates the material into the vacuum chamber. The substrate, which is located at the top of the chamber is coated by the material cloud. If the distance between the small evaporation source and substrate is large enough, the side-walls in the PMMA layer are

---

[7] Livermore, CA 94551, United States

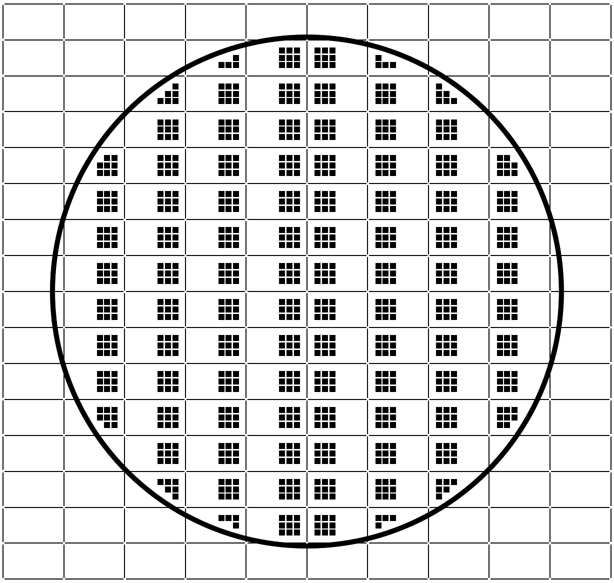

Figure 4.5: Transparency mask layout used to pattern the membrane chips. The circle marks the circumference of a 4-inch wafer.

lift-off	solution	immerse in N-Methyl-2-pyrrolidon (NMP)
	temperature	80°C
	time	about 30min
	stop	spray with NMP, Acetone, Methanol and Isopropanol

Table 4.5: Lift-off process details.

not coated and a discontinuous layer is formed. The nickel that is deposited on top of the PMMA can be removed together with the PMMA (lift-off), while the nickel in the exposed trenches remains on the substrate. The details of the lift-off step which essentially consists of immersing the sample in a solvent are given in table 4.5. Usually lift-off can be accelerated using ultrasonic agitation. However, this was avoided here since it could potentially harm the membranes.

Note that the lift-off step inverted the pattern. The material (nickel) is kept in places that were exposed by the e-beam. Alternatively, one could use a negative resist directly, and etch the nickel layer instead. This however has the disadvantage that a large area (i.e. the spaces between the support bars) would have to be exposed, which would substantially increase the time to perform the exposure step.

Tri-layer stack

For the same reason, lift-off is not suited for transferring the pattern from the zone-plate exposure. All areas away from the zone plate and part of the membrane would have to be exposed,

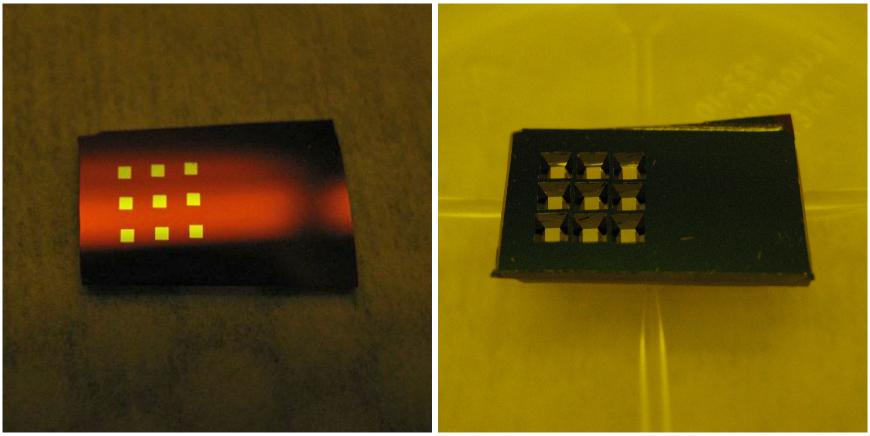
(a) (b)

Figure 4.6: Silicon-nitride coated chip with 9 membranes. (a) shows the front side which was used for processing and in (b) one can see the typical result of the anisotropic KOH etch. The tilted plane leading up to the membranes is the 111 crystal surface.

to deposit a protective coating. Also the thin PMMA layer does not withstand the long CF4 dry-etch used to etch into the silicon-nitride very well. Therefore it is necessary to transfer the PMMA pattern into a layer that can serve as a mask for the silicon-nitride etch. At the NanoStructures Lab interference lithography is a field of research. There it is common to use a tri-layer stack in order to avoid interference of the exposing laser-beam with reflections from the substrate surface. This is achieved by an anti-reflection coating (ARC), whose thickness is chosen so that reflectivity from the substrate is less than 1%. The ARC-layer is coated with silicon-oxide (SiO_2) to facilitate the dry-etch of the resist-pattern into the ARC layer. The processing steps for this tri-layer stack were well-established in the lab, which is the reason why the same procedures were adopted for the zone-plate exposure.

Pattern-transfer to silicon-nitride membrane

The zone-plate exposure was transferred to the silicon-nitride membrane in three dry-etch steps. A schematic for a dry-etcher (or reactive-ion etcher =RIE) is shown in figure 4.8. Non-reactive gas flows through a vacuum chamber at a specific rate and pressure. An RF-power-supply sparks a plasma between two parallel horizontal electrodes. The sample is located on the bottom electrode. In the plasma ions of the re-active part of the gas (for example fluor ions are produced from CF4) are formed and accelerated towards the sample. There the ions react with the surface-layer that is to be etched and remove it into the vacuum. For example, CF4 is used to etch silicon-nitride or silicon-oxide, while polymers or metals can be used to mask the etch. Fluoroform (CHF_3) is used to etch silicon-oxide, because it provides a better etch-ratio with respect to PMMA [65]. An oxygen (O_2) plasma etches polymer-layers, with silicon-oxide acting as a mask material.

The detailed settings for etching the zone-plate pattern from the PMMA layer into the silicon-

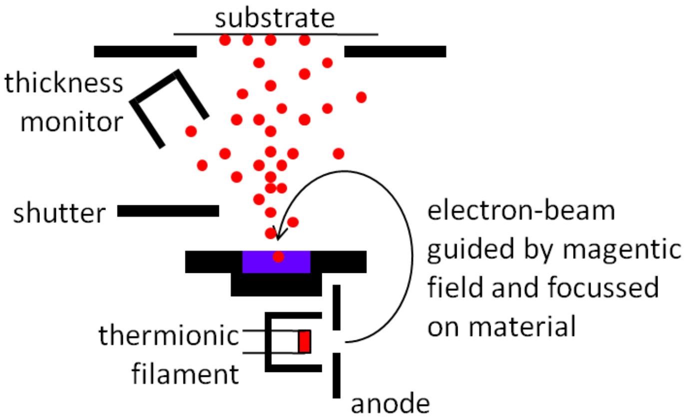

Figure 4.7: Schematic of an electron-beam evaporator.

nitride membrane are given in table 4.7. The last CF4 etch noted in the table transfers the pattern only about 3/4 down into the silicon-nitride membrane. The thick tri-layer on the membrane would otherwise tear the pattern apart due to stress between the layers. For this reason the tri-layer was first removed before turning the zoneplate pattern into a free-standing structure. This is described in the next section.

Mask-removal and final dry-etch

To keep the membrane from breaking up due to stress between the mask layer and the membrane, the mask layer was removed before the final reactive-ion etch. This was achieved by immersing the sample in a special ARC-stripper. The details are given in table 4.8. The nickel hard-mask is also removed in this bath. The ARC-stripper usually removed the ARC from the sample very well, but sometimes the ARC would stick and then withstand all efforts to remove the layer. Prolonged reactive-ion etching in an oxygen-plasma, ashing the sample in a higher pressure oxygen plasma, immersion in RCA (4:1:1 DI water:ammonium-hydroxide:hydrogen-peroxide at about 65°C) and Piranha (3:1 sulfuric-acid:hydrogen-peroxide at about 65°C) solutions all did not succeed. On such chips some of the membranes with zone-plates would break on the final dry-etch.

The final dry-etch was performed by putting the sample upside-down into the RIE chamber. To keep the membrane from touching the electrode a thin (1mm) glass slide was used to lift the sample on one side so that it was slightly tilted. The parameters for the etch were the same as in the final step listed in table 4.7, but with a reduced time of 2 minutes. To ensure that the etch really turned the zone-plate into a free-standing structure, one of the membranes on the chip can be patterned with a few zone-plate rings but without a support mask underneath. Once the etch is finished the rings will fall out and leave an open circular aperture behind.

ARC spin	material speed thickness time hotplate	Brewer Science XHRiC-11 5000 rpm 100 nm 60 s 150°C for 90 s
interlayer	material thickness tool	SiO_2 20 nm Temescal e-beam evaporator
resist spin	material thickness speed time hotplate	PMMA 950K, 1.5% in Anisole 50 nm 3000 rpm 60 s 90 s @ 175°C

Table 4.6: Parameters for coating sample that has a support hard-mask on it with a tri-layer stack.

chamber clean	tool gas flow bias voltage pressure time	Plasmatherm 790 15sccm CF4, 5sccm O_2 200V 20mT 5min
oxide etch	tool gas flow bias voltage pressure time	Plasmatherm 790 15sccm CHF3 200V 10mT 1min:15s
ARC etch	tool gas flow bias voltage pressure time	Plasmatherm 790 10sccm He and 5sccm O_2 250V 7mtorr 2min
SiNx etch	tool gas flow power pressure time	Plasmatherm 790 15sccm CF4 100W 10mtorr 7min

Table 4.7: Parameters for zone-plate dry-etch.

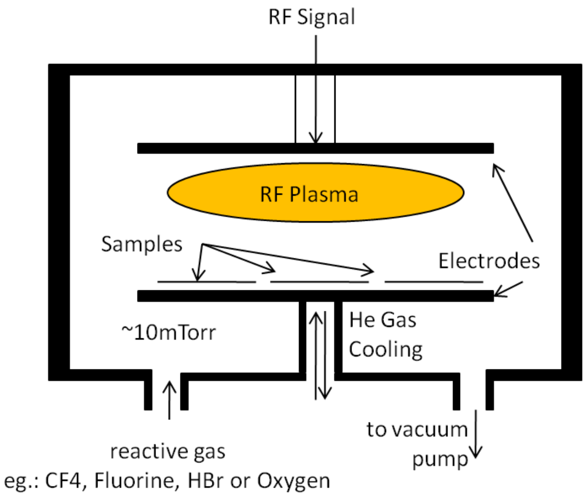

Figure 4.8: Schematic of a reactive-ion etcher.

ARC strip	solution temperature time stop	DuPont EKC265 60°C about 20min rinse with DI-water

Table 4.8: Removal of the ARC mask-layer.

4.3 Fabrication results

The zone plates which were fabricated successfully with the process described in the previous section are listed in table 4.10. The aim of the zone-plate fabrication-project was to produce zone plates for two different apparatuses. The first one is the helium-scattering apparatus that was also used in the other experiments of this thesis (Magie). The second apparatus (Nemi) is a smaller apparatus that is being assembled at the point of writing. Its aim is to obtain reflection neutral-helium microscopy images for the first time (see chapter 3). The focal length that corresponds to each apparatus is given in table 4.9. Both cold-nozzle beams (λ=97.8 pm) and room-temperature-nozzle (λ=54.7 pm) beams were assumed and thus zone plates for two different de-Broglie wavelengths were fabricated. The densest grating patterns correspond to the short-wavelength zone-plate for the room-temperature-nozzle beam.

apparatus	source distance g / mm	detector distance b / mm	focal length f / mm
Magie	1500	700	477.3
Nemi	935	205	168.1

Table 4.9: Optical path distances for the two helium beam apparatuses.

chip	mem	$\varnothing_{ZP}$/µm	$\varnothing_{stop}$/µm	f/mm (λ/pm)	dr$_n$/nm	N	τ / %	η / %
#5	#5	188	60	477.3 (100)	289	166	59±3	7.7±0.3
	#6	188	60	477.3 (100)	289	166	55±3	9.5±0.3
#6	#4	188	60	477.3 (97.8)	323	170	-	-
	#5	188	60	477.3 (97.8)	323	170	58±4	9.0±0.4
	#6	188	60	477.3 (54.7)	202	304	67±2	7.3±0.3
	#8	188	60	477.3 (54.7)	202	304	68±3	7.5±0.5
#8	#1	192	20	168.1 (97.8)	125	554	-	-
	#2	192	20	168.1 (54.7)	51	991	-	-
	#3	192	20	168.1 (97.8)	125	554	-	-
	#5	192	20	168.1 (54.7)	51	991	-	-
	#6	192	50	168.1 (54.7)	51	934	-	-
	#8	192	50	168.1 (54.7)	51	934	-	-
	#9	192	50	168.1 (97.8)	125	522	-	-
#9	#2	160	60	477.3 (97.8)	325	118	47±6	9.9±0.5
	#5	388	140	477.3 (97.8)	157	701	55±1	7.8±0.1
	#8	160	60	477.3 (54.7)	187	211	56±3	9.1±0.7

Table 4.10: List of fabricated zone plates and their parameters. 'mem' refers to the membrane number as assigned in figure 4.9(a). $\varnothing_{ZP}$ is the zone-plate diameter and $\varnothing_{stop}$ is the diameter of the central blocking disc. f is the focal length of the zone plate at wavelength λ. dr$_n$ is the width of the outermost zone, and N is the total number of patterned zones. τ and η are the transmissivity and efficiency, respectively, as measured by Martin Greve [38].

For chips #5 and #6 the process deviated slightly. For example a thicker ARC coating was used (AZ BARLi ARC[8]) which was available as a more concentrated fluid, resulting in thicker layers (about 200 nm at 6000 rpm spin-speed). The later zone plates were fabricated using the thinner XHRiC coating, to prevent high aspect ratios at the outermost zones of the short-focal-length zone-plates.

The Magie zone-plates were tested as part of Martin Greve's Master Thesis [38]. The measured transmissivities and efficiencies are listed in table 4.10 together with the other zone-plate parameters. The transmissivity refers to the ratio between the total beam-intensity passing through the zone plate and the total intensity incident on the zone plate. It it used to test if all the open zones of the zone plate are completely transparent and also if the ratio between closed and open zones is 50% (open-ratio). The diffraction efficiency of the first diffraction-order is the ratio between the total intensity measured in the first diffraction order and the incident total intensity. For all of the zone plates for which this was measured (see table 4.10), it corresponds surprisingly well to the expected efficiency, if one takes into account the measured open-ratio (see equation 3.11) and the area covered by support bars. There were two exceptions.

The first is the zone plate on chip #5, membrane #5. It should have an efficiency in the uncertainty interval 9.3±0.5. Unfortunately, it is possible that the two zoneplates on the chip were confused during the measurements or the fabrication. We know that one of the zone plates

---

[8] AZ Electronic Material Services Ltd, Stockley Park, UB11 1BD, UK

on the chip was ’corrected’ with the distortion map from the Lloyds-mirror fiducial-grid. We suspect that the grid is not as precise as expected (see figure 4.20), so it is highly likely that the measurement with the reduced efficiency corresponds to the zone plate with the falsely corrected zone-plate pattern.

The other exception is the large 388-µm-diameter zone-plate. It should have an efficiency of 9.9±0.1. Here it is clearly the stitchting-errors that are reducing the zone-plates’s efficiency. The image in figure 4.2 shows part of the stitching error of that zone plate.

It was also attempted to measure the efficiency of the Nemi-zone-plates using the Magie apparatus, by allowing a large distance between scanning-slit and detector and thereby moving the imaging plane closer to the source and zone plate. This however resulted in unexpected variations of the detector signal, even when measuring the direct beam. Therefore, the efficiency measurements for those zone plates were postponed until the completion of the Nemi-apparatus.

The zone plates on chip #5, membrane #6 and on chip #6, membranes #5 and #8 are different in the sense that the patterns input to the Raith lithography-software have been intentionally distorted to counter-act intra-field distortion (using the script in appendix B.1). An intra-field distortion-map has been measured using an interference-lithography grid, as described in section 4.4.3, and was then inverted and used to distort the zone-plate pattern-file. The efficiency measurements so far have not been precise enough to clearly establish that the patterns of those zone plates are closer to that of an ideal zone-plate. A better way to do this would be to precisely measure the focus width with a more intense beam (using a micro-skimmer with a few tens of µm diameter) and 2-dimensional scans of the beam-focus. If that does not yield a definite answer, it would be possible to measure the third-order focus, which depends much stronger on the pattern-fidelity of the zone plate (see section 3.1.3 or Takeuchi et al. [89]).

The large four-write-field zone-plate (chip #9, membrane #5) has been used already to measure the virtual-source size of a deuterium (D_2) supersonic-expansion beam. This is the topic of paper E and is discussed in chapter 5.

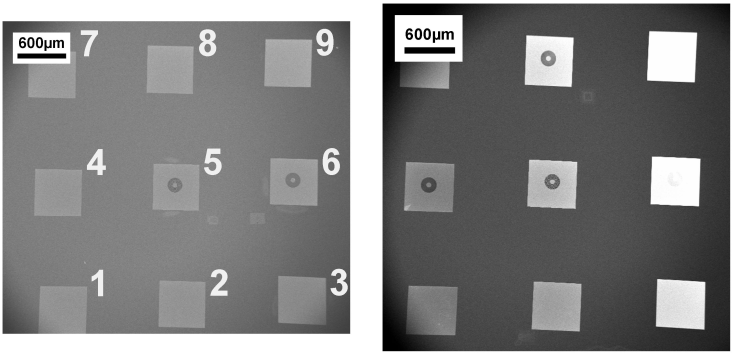

(a) chip #5

(b) chip #6

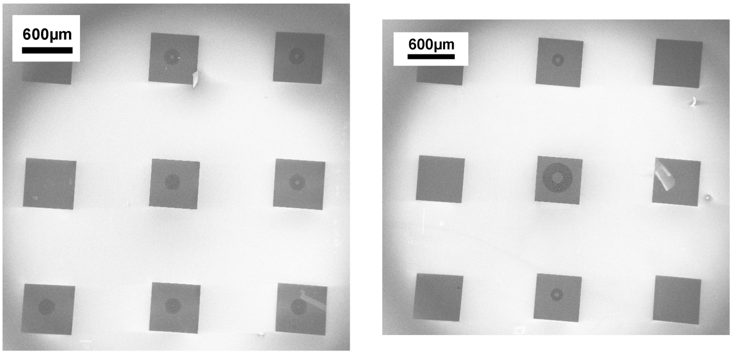

(c) chip #8

(d) chip #9

Figure 4.9: Scanning-electron micrographs of the membranes on four chips with zone plates. The image in (a) is marked with the membrane numbers as they are used in this thesis. The orientation of the chip is so that the empty part of the chip, which is meant for handling it, is to the right. Chip #5 has two cold-beam Magie zone plates. Chip #6 contains two cold-beam and two room-temperature beam zone plates. One of each was corrected for write-field distortion. Chip #8 contains seven Nemi zone plates. On chip #9 one can see the large 4-field Magie zone-plate beside two smaller Magie zone plates.

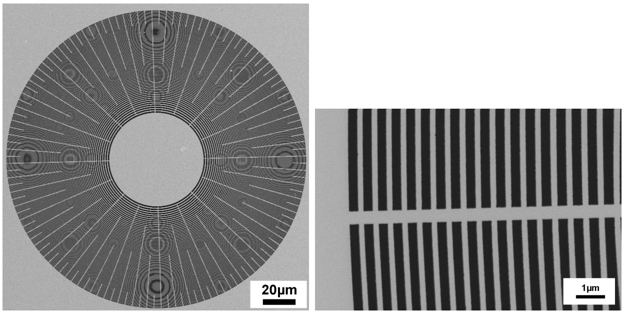

(a) (b)

Figure 4.10: Chip #6, membrane 5. (a) shows the zone plate as a whole and in (b) one can see the resolved outermost zones.

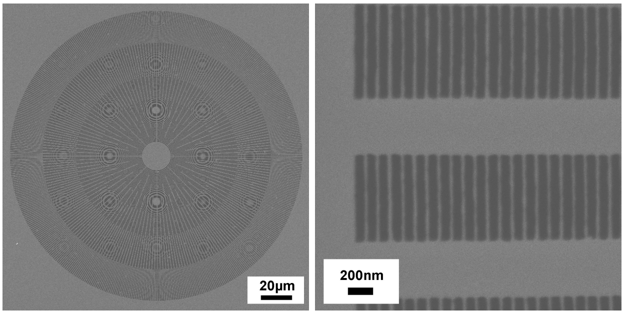

(a) (b)

Figure 4.11: Chip #8, membrane 5. (a) shows the zone plate as a whole and in (b) one can see the resolved outermost zones.

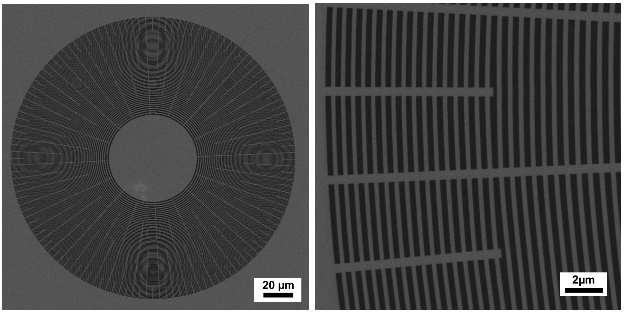

(a) (b)

Figure 4.12: Chip #5, membrane 5. (a) shows the zone plate as a whole and in (b) one can see the resolved outermost zones.

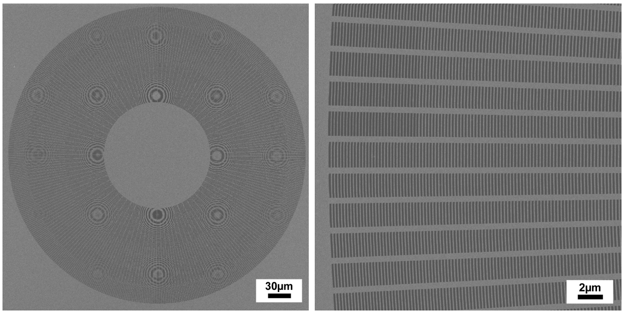

(a) (b)

Figure 4.13: Chip #9, membrane 5. This is the 388-µm-diameter zone-plate that was patterned with four write fields. (a) shows the zone plate as a whole and in (b) one can see the resolved outermost zones.

4.4 Spatial-phase-locked electron-beam lithography

In section 4.1.2 it was explained that pattern-placement in conventional EBL is not as good as implied by the precise positioning of the substrate with the interferometric stage. This section discusses the use of reference grids (fiducial grids) to overcome some of the mentioned sources of error. In section 4.4.1 I show how a precise reference grid can be fabricated using interference-lithography. The actual process that was used to fabricate a grid that can be imaged with enough signal-to-noise ratio is discussed in section 4.4.2. This grid is then used in two ways. First the intra-field distortion of the 200-µm write-field was measured using linescans of the grid. This distortion measurement can then be applied as a filter to the zone-plate patterns, to reduce systematic errors in the deflection of the beam. This method is covered in section 4.4.3. The second way consisted of segmenting the grid such that it would only remain in areas not important to the zone-plate pattern (i.e. the corners of the write-field). This way the grid can be used during the exposure to repeatedly re-align the write-field to the substrate, with the segmented grid essentially functioning as precise alignment marks. The process of segmenting the grid is documented in section 4.4.4 and its application in section 4.4.5.

The methods applied here to zone-plate fabrication were developed by J.T. Hastings [43], F. Zhang [96] and J. Ferrera [29] under the supervision of H.I. Smith at the NanoStructures Laboratory. I performed the interference lithography exposures on the Mach-Zehnder interferometer at MIT's Space Nanotechnology Laboratory [55].

Unfortunately, the full potential of these techniques could not be demonstrated as part of this project. It is hoped that this documentation will however serve as a guideline for future projects. Eventually, spatial-phase-locked EBL (SPLEBL), which refers to the locking of the e-beam's position to the reference grid, promises to provide placement-accuracy on the nanometer level.

4.4.1 Interference lithography

The reference grid must be of sufficient resolution and have better long-range spatial-phase coherence than the EBL system. One option to fabricate a grid with these properties is to utilize the phase of high-coherence laser-radiation as a reference standard. In an interferometer two coherent laser beams can be used to form a linear grating pattern of high spatial coherence. By exposing a resist-coated substrate to this interference pattern a physical grating can be fabricated. The grating can be turned into a grid by repeating the exposure after turning the substrate by 90° in the interference plane.

The spatial coherence of the interference pattern that is formed when two coherent laser beams are overlapped depends on the uniformity of the wavefronts of the interfering beams. Even with lasers it is difficult to produce high-quality wavefronts of large extend. One way to overcome this problem is to combine a small-area interference pattern with a high-precision interferometric stage. The interference pattern can be scanned over large areas without the loss of spatial coherence [55].

Since the zone plates to be fabricated here only cover small areas (less than 1 mm square) the spatial coherence from interfering two spherical wavefronts would suffice [30]. The interference-lithography setup used here is depicted in figure 4.14. It is a Mach-Zehnder interferometer [55] that uses an argon-ion laser with a wavelength of 351 nm as source (0.5W). The laser was located on a separate optical table and locked onto the beam-path of the interferometer setup via piezo-driven mirrors and a feedback-loop involving quadrant photo-sensors (not shown in the schematic). A beam-splitter directs the beam onto two mirrors which are approximately 2m apart. The spherical wave-fronts are produced in two spatial filters, where the beam is focused onto a 5-µm-diameter pinhole. The resulting beam-radii are about 1m. Due to air-convection and vibration the path-lengths of the two interferometer arms vary over time. For this reason is was important to lock the phase-relationship between the two arms. This is accomplished by changing the phase of one of the arms, by sending it through a Pockels cell [55] which is controlled by two phase detectors located just above the substrate. The beam power in the two interferometer arms is balanced using a variable attenuator. Unwanted reflections of the beam onto the substrate are avoided by placing the gaussian beams produced by the spatial filters in dark-matted horn-shaped channels. This way an area corresponding to a 4-inch wafer can be exposed with a grating pattern. The substrate holder can be rotated with a nonius to measure the angle for grid production.

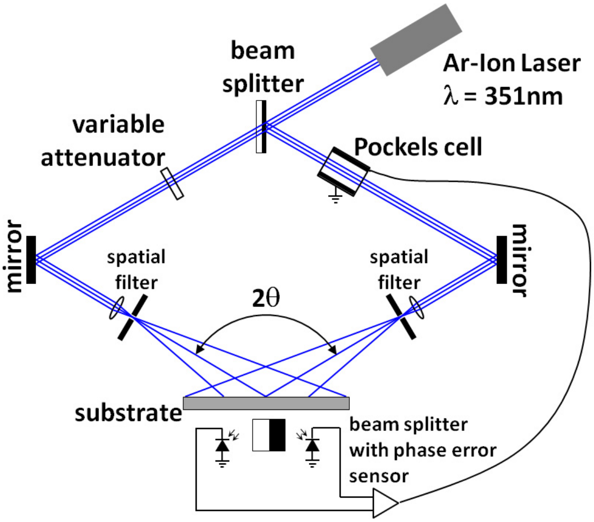

Figure 4.14: Mach-Zehnder interference-lithography setup (after Konkola [55]).

The resulting period of the interference pattern depends on the wavelength of the laser beam and the angle subtended by the two interferometer-arms:

$$p = \frac{\lambda}{2sin(\theta)} \tag{4.2}$$

Since the wave-fronts are not planar the interference pattern is distorted hyperbolically. The error in the long-range spatial-phase coherence is less than 100 nm in an area of less than 1cm^2 [29]. The zone plates patterned here only cover areas of 400-µm square, which means that one can expect the grids produced here to be superior in precision compared to the EBL system. For even better precision the hyperbolic error could be overcome by using the scanning interference-lithography method as described before.

adhesion promoter application	material method time thickness	HMDS cover substrate, spin-off after wait 30-60s monolayer
photo-resist spin	material thickness speed time post-spin bake	PS4 200 nm 5000 rpm 60 s 90 s @ 90°C
develop	material post-exposure bake time stop	Microposit MF CD-26 90 s @ 110°C immerse 60 s @ room-temperature rinse with DI-water

Table 4.11: Parameters for coating silicon-oxide-coated sample with negative-tone photo-resist.

4.4.2 Fiducial grid fabrication

The full fabrication process I used is given in figure 4.15. I used a negative-tone and chemically amplified photo-resist (OHKA THMR-iN PS4[9]). The parameters for the tri-layer (see figure 4.17) are the same as in table 4.6. Parameters for spin-coating PS4 and the development process are given in table 4.11. Note that PS4 photo-resist has bad adhesion properties on silicon-oxide (silicon-oxide surfaces are hydrophilic). For this reason an adhesion promoter, hexamethyl-disilazane (HMDS), is applied before spin-coating with the photo-resist.

The photo-resist-coated substrates were exposed for 50 seconds at each of the two orientations. The beam power at the substrate was 0.22 mW. Note that it is important to align the wafer-flat with the stage, so that it is easy to align with the grating in any of the later process steps. To ensure that the exposures would be at exactly 90° we used a Michelson interferometer with a helium-neon laser, a beam-splitter cube and an optically flat mirror. The laser was reflected from one of the short sides of a precision glass prism (the two short sides subtend an angle of 90°±1'). The prism is rotated with the substrate on the precision-rotation stage. After 90° rotation the laser-beam is reflected of the second short side of the prism back into the interferometer. Based on the orientation of the fringes projected onto a screen, it was possible to turn the substrate by 90° with a precision of about 1 arc-minute.

After development the photo-resist pattern (a grid of holes - see figure 4.17) was transferred into the ARC layer with the same RIE recipes as given in table 4.7, but without the final step (the pattern is not etched into the silicon-nitride layer). The grid was then coated with 10 nm aluminum plus 50 nm gold in the Temescal e-beam evaporator. Gold was chosen because of its high secondary-electron yield, resulting in good imaging contrast. The aluminum served as an adhesion layer, since gold alone does not stick very well to surfaces like silicon or silicon-nitride [35]. The final step was a lift-off step in which the ARC layer was dissolved. This

---

[9] Tokyo OHKA KOGYO CO. LTD.,150 Nakamaruko, Nakahara-ku, Kawasaki-shi, Kanagawa Prefecture 211-0012 Japan

was done with the same recipe as shown in table 4.8. No additional agitation was necessary to remove the layer, leaving behind dots of aluminum-gold. Initially an adhesion layer of titanium was used instead of aluminum. The ARC-stripper EKC265 however demonstrated a fairly high etch-rate for titanium, lifting-off some of the gold dots and displacing them randomly.

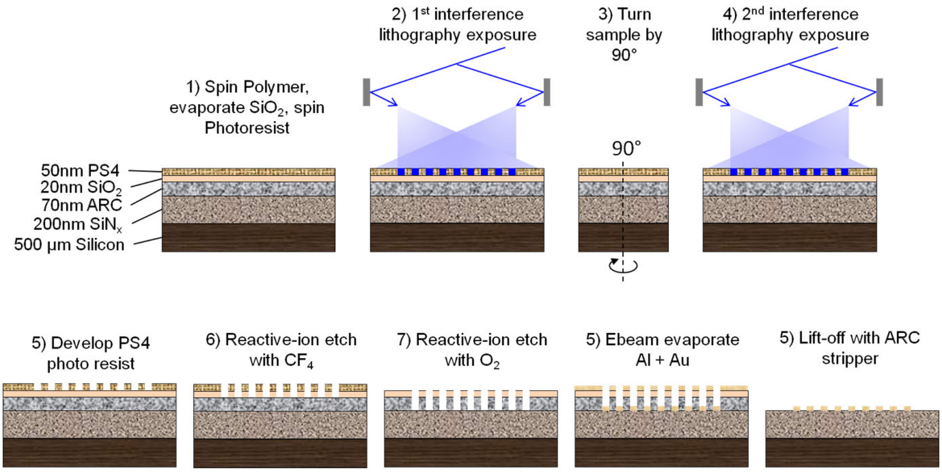

Figure 4.15: Fiducial grid fabrication process.

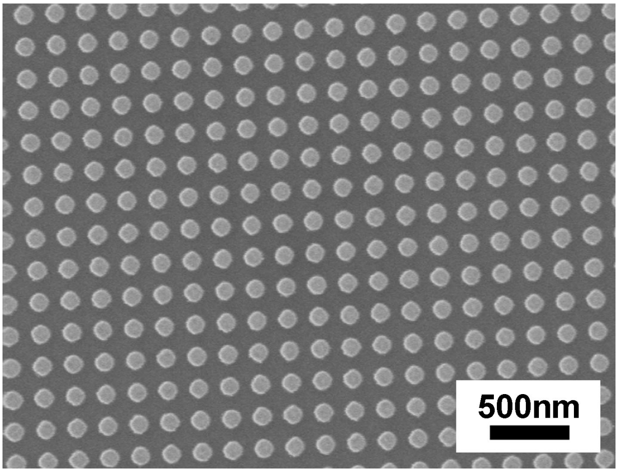

Figure 4.16: Scanning-electron micrograph of an aluminium-gold fiducial grid on silicon-nitride-coated silicon-wafer. The period of the grid is 200nm.

4.4.3 Intra-writefield distortion

The fabricated fiducial grid with a period of 200 nm can be used to measure the distortion of the write-field by imaging it. The measured distortion map in part represents errors that

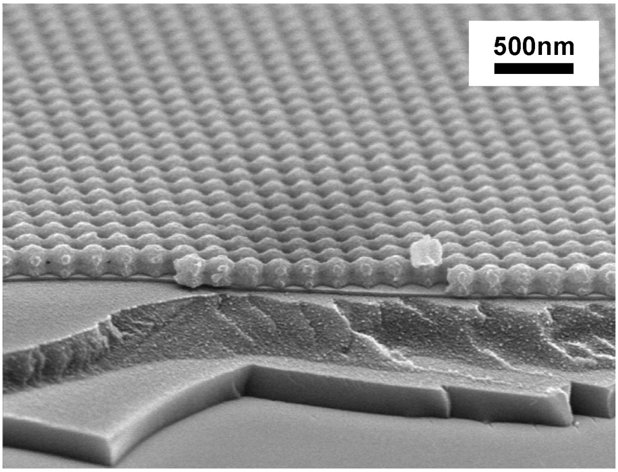

Figure 4.17: Scanning-electron micrograph of an ARC-SiO_2-PS4 tri-layer with 200-nm period grating exposed with the Mach-Zehnder interferometer. The chip was cleaved and the image shows the edge of the cleaved chip at an angle. The layers have broken at different places so that they are especially easy to distinguish. Unfortunately, the exposure shows a fair amount curvature due to standing waves, which should have been avoidable with the correct thickness of the ARC-coating.

are repeatable and thus can be corrected by distorting the intended pattern in the opposite directions. However, imaging the entire write-field at high enough resolution to resolve the grid and at beam speeds that correspond to the actual exposure beam-speed is not feasible. Taking such a slow measurement of the distortion would not accurately represent the intra-write-field errors that occur during the exposure, since the write-field would drift already during the measurement. This slow drifting cannot be corrected by a simple imaging method. It is only the systematic errors that can be corrected this way. It is therefore important to speed-up the measurement of the distortion. This can be achieved in one of two ways. With sparse-sampling [42] one can deduce the write-field distortion from the distortion of the Moiré-pattern that results when the field is imaged at a resolution that is too low to resolve the reference-grid. The second method involves dividing the writefield into a number of subfields akin to a chessboard, and determining the placement deviation in each field from a vertical and a horizontal line scan. The distortion map for the full write-field is then interpolated from the placement-error of each subfield. The latter approach was chosen here.

The distortion-map that was used to correct the patterns of the zone plates on chip #6, membranes #5 and #8, is shown in figure 4.19. It was created by dividing the 200-µm writefield into 8-µm squares. The horizontal and vertical linescans spanned each square (i.e. had a length of 8µm) and crossed at the center of each square. The linescans were averaged over a width of 192 nm to ensure that the linescans would not be taken just between the dots of the grid. The resolution of each linescan was 3.2 nm along the direction of the scan. An x-line-scan is shown in figure 4.18. The phases of the linescans were obtained in a Matlab script by taking the fourier transform after applying a hanning-window. The deviation from the expected phase had to be calculated by taking some random reference point. The square at the center of the write-field was chosen for this purpose (The writefield is spanned by 25 by 25 squares).

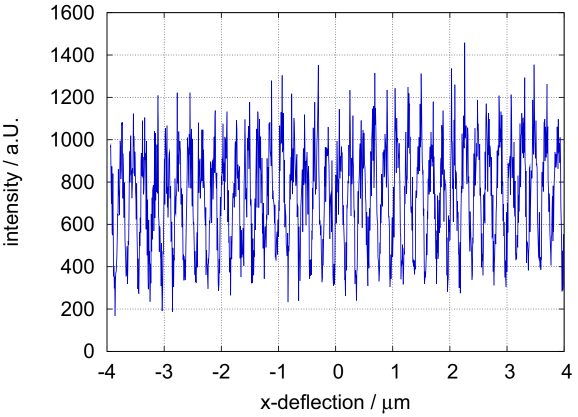

Figure 4.18: X-linescan of the bottom left field in the write-field. The placement error in x corresponding to that field was calculated by determing the phase of the signal using Fourier transformation.

The zone plate on chip #5, membrane #6 was corrected with a distortion-map that was acquired from a different grid-sample which was fabricated using a Lloyds mirror interference-lithography setup (which can be implemented at low cost [33]). It was later found out that grids created with this holography method do not necessarily have the expected long-range precision. The precision of the interference pattern created by a Lloyds mirror interferometer is determined by the flatness of the mirror and also affected by reflections from dust particles. Such distortions of the ideal interference pattern from dust particles show as point holograms on the finished grid which are readily visible in an optical microscope. For this reason it was decided to attempt the fabrication of a reference-grid using a Mach-Zehnder interferometer. The grids fabricated using that method did not suffer from the same distortion as could be checked in an optical microscope - see figure 4.20.

4.4.4 Segmented fiducial-grid fabrication

With the aim of reducing inter-write-field distortion I also attempted to fabricate zone-plates aligned to a segmented fiducial-grid. This means that the reference grid is reduced to cover locations that are non-essential to the zone-plate pattern. The intended layout is shown in figure 4.21. During exposure of each write-field the grid-marks are scanned frequently in x and y directions to obtain small corrections to the alignment-parameters of the the write-field.

The segmentation of the 200-nm-period grid was performed by means of contact UV-lithography (tool: OAI contact-aligner). The four-inch wafer with the gold fiducial-grid was first cleaved into smaller pieces to facilitate good contact during the exposure step. The segmentation pattern consisted of 10-µm squares in a grid pattern of 200 µm period. The mask used to expose the segmentation pattern was a chrome-quartz mask ordered from Benchmark Technologies[10]. The parameters to spin photo-resist, develop it after exposure and etch the aluminum-gold dots not covered by resist are detailed in table 4.12. The etchants used were

---

[10] http://www.benchmarktech.com, Benchmark Technologies, 7 Kimball Lane, Bldg. E, Lynnfield, MA 01940,

resist	type spin speed thickness bake	Microposit S1813 60 s at 5000 rpm $\approx$ 1200 nm 120 s at 90°C
exposure	tool time	OAI contact aligner 7 s
development	solution time and temperature stopper solution stopping time	MF 321 rinse for 60 s at room-temperature de-ionized (DI) water rinse for 120 s
gold wet-etch	material time stop	Transene TFA gold etch 30 s at room temperature rinse in DI-water
gold wet-etch	material time stop	Transene type A aluminium etch 10 s at room temperature rinse in DI-water
remove resist	tool time power gas mixture	Technics PlanarEtch II (Asher) 12 min 100W He + 20% O_2

Table 4.12: Contact UV lithography to fabricate segemented grid.

supplied by Transene[11]. Following the wet-etch I removed the resist with an oxygen plasma. This also ensured that the grid would be clean for further use in the zone-plate process. A scanning-electron micrograph of one of the grid marks is shown in figure 4.23(a).

The process steps to get a zone plate using the segmented fiducial grid were only attempted once and were not particularly successful. Also the alignment to the segmented grid did not work well (see next section). What was attempted was to create a hard-mask of nickel aligned with the segmented grid (see figure 4.23(b)) as for all other zone plates. Then coat the wafer with a thick spin-coatable layer (Brewer Science ProTEK 3B-25[12]), which would protect it during the long KOH wet-etch. This worked only to some extend. Some of the patterned support hard-masks got removed in the KOH etch, as the protection layer lifted off. Also the removal of the layer was problematic afterwards. The recommended stripping procedure did not remove the layer. A long oxygen plasma-etch on the RIE eventually removed the layer, and I proceeded with the remaining process-steps (tri-layer application) before attempting to pattern a zone plate aligned to the segmented fiducial-grid. Locking the write-field to the segmented grid however remained problematic.

In a future adaptation of this process it would be better to partially (75% etch-depth) transfer the full zone-plate pattern into the silicon-nitride layer before the KOH etch. This implies that dose-algorithm determining the zone-widths would need to be re-calibrated, since the patterning would take place on the full silicon substrate. An important addition to the process would also be an adaptation of the support hard-mask. It should additionally cover the places of the segmented grid, as the grid-marks are unavoidably exposed during the line-scans. The line-scans need to be slow in order to be precise and therefore also deposit a substantial amount of dose. The fact that the segmented grid-marks were located underneath the tri-layer further reduced the signal-to-noise ratio in the line-scans.

4.4.5 Zone-plate patterning with a segmented fiducial-grid as reference

Aligning the write-field to the segmented-grid is accomplished with a combination of a Visual Basic script and a Matlab script. The visual basic script automates the exposure and scanning procedures on the Raith-150. The Matlab script calculated the correction for the write-field position based on the line-scans. Refer to Appendix B.2 for a listing of the mentioned scripts.

The locking to the segmented fiducial-grid did not work fully by the end of this project. I suspect the main reason for this is that the variable errors in the 200-µm write-field close to its edges were larger than expected. The observed effect was that the write-field would frequently be displaced by a whole period of the segmented grid. A possible solution to this is to use a larger write-field, or reduce the area to be patterned within the write-field. Then the segmented grid marks would have to be enlarged in size and moved closer together. The choice of a 200-nm-period grating was probably also too optimistic. While the small period offers better precision, it also limits the maximal error that can be corrected for.

USA

[11] Transene company Inc., Danvers Industrial Park, 10 Electronics Avenue, Danvers MA 01923, USA.

[12] Brewer Science, Inc., 2401 Brewer Drive, Rolla, MO 65401 USA

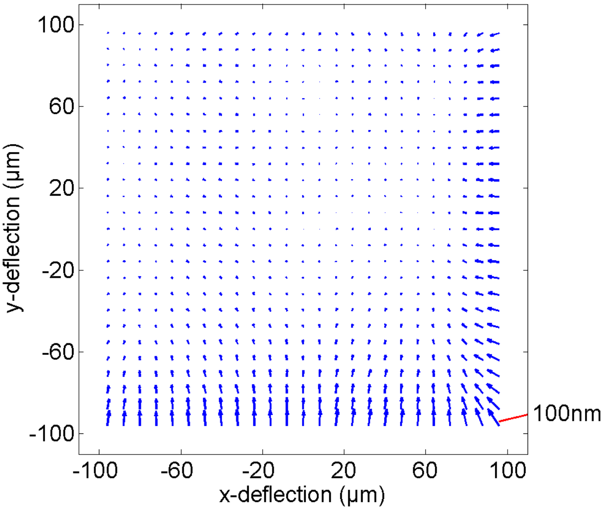

(a)

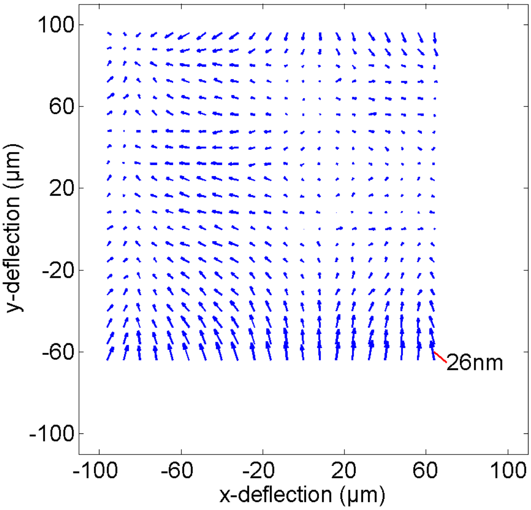

(b)

Figure 4.19: Intra-writefield distortion-map of a 200-µm writefield measured with a Mach-Zender interference-lithography grid. The arrows correspond to the error in placement at each subfield. Each subfield is 8 µm by 8 µm. The map is the average of three separate scans. (a) shows the full map while in (b) the less distorted upper-right of the field is shown with a larger scaling of the arrows. The large deviations at the bottom and right-hand edges of the field are probably caused by 'fly-back' of the beam between line-scans. It has not been possible so far to show that these errors do not occur during the circular zone-plate exposures.

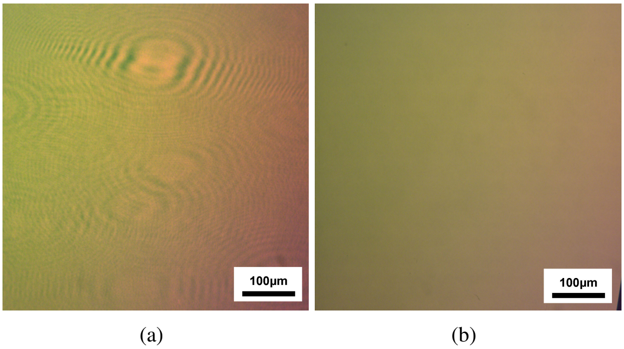

(a) (b)

Figure 4.20: Fiducial grid as seen through an optical microscope. The grid in (a) was fabricated with a Lloyds Mirror interferometer and the grid in (b) was fabricated with a Mach-Zehnder interferometer.

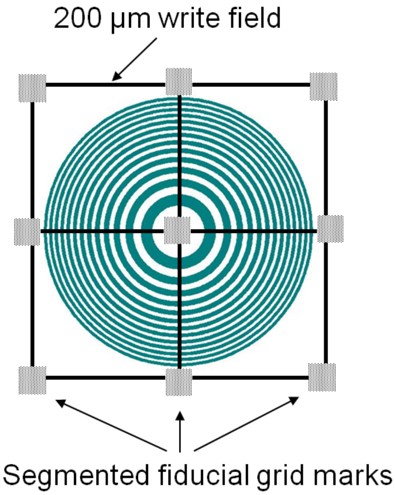

Figure 4.21: Zone-plate patterning with a segmented fiducial-grid as a reference.

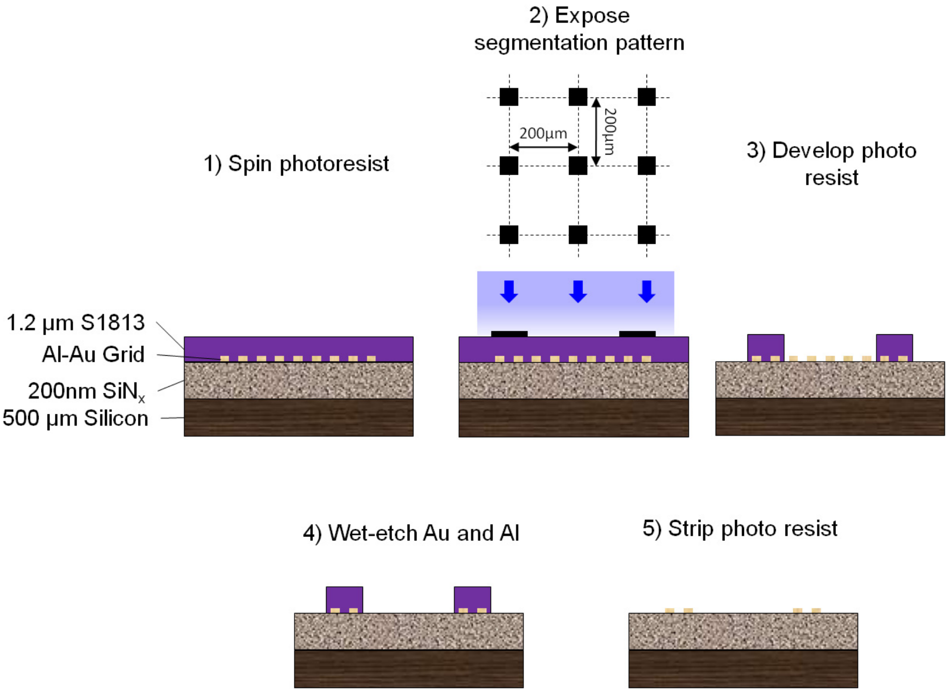

Figure 4.22: Grid segmentation process.

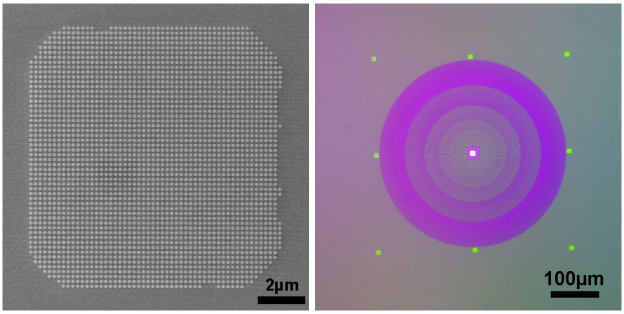

(a) Scanning-electron micrograph of segmented grid mark

(b) Zone-plate-support hard-mask with segmented grid

Figure 4.23: Segmented grid.

Chapter 5

Supersonic expansion of deuterium gas (Paper E)

In paper E we image the virtual source [6, 78] of a supersonic expansion of normal molecular deuterium (D_2) using two Fresnel zone-plates. This illustrates another application of free-standing Fresnel zone-plates, beside neutral-helium microscopy (see chapter 3). In the paper the beam's energy distribution is additionally characterized with time-of-flight methods. The three parameters thus obtained, namely the virtual-source width, the terminal speed and the terminal speed ratio can be used to deduce the perpendicular temperature, the kinetic energy and the parallel temperature of the beam, respectively. The latter parameters are compared to a theoretical model that numerically solves the Boltzmann equation to predict the final velocity distribution and explicitly includes the coupling between translational and rotational degrees of freedom (Formulated and implemented by G. Bracco). The correspondence between experiment and model is very good.

In addition we observe clustering in the beam which results in a deviation of the experimental data from the model, since the model does not account for any condensation in the beam. The condensation of the molecules releases additional energy into the expanding gas which affects the final temperature and kinetic energy of the beam. By assuming a value from literature for the specific heat of vaporization at the triple point of deuterium we could estimate the fraction of condensed molecules in the beam from the deviation between experiment and model.

The characterization of supersonic-expansion sources in general is important due to their applications in a wide spread of scientific fields [82]. First there are the examples discussed in this thesis: the field of De-Broglie matter-wave experiments which the experiment in chapter 2 falls into and matter-wave microscopy which was the subject of chapter 3. Supersonic-expansion beams are also useful in surface science [28] where the beam is usually scattered off samples to retrieve information on the structure and dynamics of the surface. The apparatus used in this thesis for example has made important discoveries about the surface structure and dynamics of alpha-quartz [86, 87] and glass [88]. At low nozzle temperatures and high pressures the gas atoms or molecules can condense to form weakly-bound clusters, first observed by Becker et al. [5]. Their sizes reach from dimers to microdroplets or micro crystals with 10^6-10^7 particles [70]. Cluster beams have found many applications such as for example the fueling of fusion reactors [61] and cluster beam deposition [57].

The supersonic expansion of normal D_2 has been studied recently by Ekinci et al. [27], which is complemented very well by paper E especially since the experiments there were performed on an apparatus very similar to the one used here. The source was studied in paper E for the following parameter: nozzle temperature T_0=310 K with the pressure range p_0=2 bar-170 bar and T_0=106 K with the pressure range p_0=2 bar-130 bar.

In section 5.1 I present a brief background on supersonic expansion beams and discuss the corresponding results in parallel. Section 5.2 outlines the specifics of the experimental setup that were used in the deuterium expansion measurements. Finally, section 5.2.2 explains the model for the zone-plate focus in a little more detail than the paper does. At the end of the chapter the results from paper E are summarized.

5.1 Supersonic expansion beams

In a supersonic-expansion, also referred to as a free-jet expansion, compressed gas flows through a short converging nozzle into vacuum. Due to the pressure differential between the reservoir (p_0) behind the nozzle and the vaccum chamber (p_a) the gas accelerates towards the opening in the source. Initially the expansion is governed by continuum flow and it can be described as an isentropic expansion where friction and heat conduction can be neglected [70]. As the density of the gas quickly decreases the gas increasingly reaches a state of non-equilibrium due to an increase in the mean-free-path. Collisions which determine kinetic processes like cooling of internal states, decrease at the same time and eventually cease completely. At that stage the gas has attained a regime of free molecular flow, where the mean-free-path is larger than the apparatus dimensions. In the sudden freeze model [1, 70] of the expansion the transition to molecular flow occurs at the so-called quitting surface. Beyond the quitting surface the temperature of the beam is defined using the velocity distributions perpendicular and parallel to the beam. The parallel temperature remains constant beyond the quitting surface, while the perpendicular temperature further reduces due to geometrical cooling. The latter effect is however purely due to the $\frac{1}{r^2}$ divergence of the beam, and hence an artifact of the temperature definition. The zone-plate focusing which was used to measure the perpendicular temperature at the quitting surface reverses the geometrical cooling effect.

The expansion converts the stagnation enthalpy of the gas in the source reservoir into kinetic energy. So in general for atomic expansions parameters like the intensity of the beam and the terminal speed parallel to the beam axis can be estimated using the ideal gas equations. For helium however especially the speed-ratio deviates from such considerations. This is due to a quantum-mechanically founded increase in the collision cross-section of the expanding gas [13]. For molecular expansions the additional degrees of freedom must be considered such as rotation and vibration. They require a certain number of collisions to reach equilibrium with the translational degrees of freedom. If a molecule experiences less than that number of collisions during the expansion the states of that degree of freedom will remain unchanged. This is the case for vibrations in the D_2 expansion we have studied here. However, rotation does play a role and had to be included in the model used to predict the measured parameters of the expansion.

5.1.1 Beam intensity

The beam intensity from a supersonic-expansion source decreases with the square of the distance. For a source where the skimmer does not obstruct the virtual source (see section 5.1.4) the density n is approximately given by the following equation [63]:

$$n = 0.155\, n_0\, (\frac{d}{x})^2. \tag{5.1}$$

where x is the distance from the source, d is the diameter of the nozzle and n_0 is the density of the gas at the nozzle. The latter can be calculated to good approximation - even at the high nozzle pressures used here - with the ideal gas law:

$$n_0 = \frac{p_0}{k_B T_0}. \tag{5.2}$$

where p_0 and T_0 are the nozzle pressure and temperature, respectively. k_B is the Boltzmann constant. From equation 5.1 one can calculate the expected count-rate N at the detector to be

$$N = n\, v_\infty\, A\, f_{eff} \tag{5.3}$$

where v_∞ is the terminal speed, A is the area of the detector entrance aperture and f_{eff} is the efficiency of the detector. If the skimmer restricts the virtual source, the intensity measured at the detector is proportional to the area of the skimmer opening. This implies that the detector count will reach a maximum when the size of the virtual source is about the size of the skimmer opening. This was important in the focusing experiments of paper C as well as the Poisson spot experiment. In both cases a small glass-skimmer [10] restricted the virtual-source size.

Furthermore, the intensity will deviate from the linear relationship with nozzle-pressure p_0 if the pressure in the vacuum chamber p_a reaches high levels due to limited pumping speed. Then scattering between beam particles and particles from the background gas can reduce beam intensity. This occurs at nozzle-pressures above about 100 bar for a room-temperature source on the apparatus used in this thesis.

5.1.2 Terminal speed

The terminal speed of the supersonic-expansion beam can be estimated by considering energy conservation [27]:

$$h_0 + (1-x)\Delta h_{lg\infty} = h_{trans\infty} + e_{rot\infty} + \frac{1}{2}u_\infty^2 \tag{5.4}$$

The left-hand-side of the equation represents the energy per mass of the gas in the source and due to condensation while the right-hand-side gives the energy per mass after expansion. h_0 is the stagnation enthalpy including rotational energy at the source. x is the fluid quality in the jet so that $1-x$ is the fraction of condensed molecules. $h_{lg\infty}$ is the specific heat of condensation (or vaporization). The second term is thus the energy released in the condensation process. $h_{trans\infty}$ is the random translational enthalpy and corresponds to the parallel temperature of the beam which is characterized by its speed-ratio. The terminal rotational energy is referred to as $e_{rot\infty}$ and u_∞ is the terminal speed.

For the expansion of helium condensation is negligible even at the lowest source temperatures that can be achieved with the apparatus used here (T_0=100K) and there is no rotational degree of freedom. The contribution from random-translational enthalpy is estimated to be less than 1% [27] and is definitely smaller for helium than it is for deuterium, due to the high speed ratios that can be attained with helium. From kinetic gas theory we know that the internal energy of an ideal gas is $U = \frac{3}{2}k_BT$. Enthalpy H is defined by $H = U + pV$ which can be written as $H = U + k_BT$ for an ideal (per particle). Hence, assuming that the gas is cooled substatially in the expansion, we can write for the terminal speed:

$$v_\infty = \sqrt{\frac{5k_BT_0}{m}} \tag{5.5}$$

where m is the mass of the particle.

In the case of D_2 the rotational degree of freedom needs to be taken into account (see paper E for details of the model by G. Bracco). In the model that we use to describe the expansion the temperatures and speed of the beam at the quitting surface are calculated by solving the Boltzmann equation [70]. The experimental terminal speed results are summarized in tables 5.2 and 5.1.

5.1.3 Terminal speed ratio

The speed ratio of an atomic or molecular beam is defined by

$$S^2 = \frac{1/2mu_\infty^2}{k_BT_{||}}. \tag{5.6}$$

where $T_{||}$ is the temperature of the beam parallel to the beam axis. Note that u_∞ is also parallel to the beam axis. The definition is based on the Maxwell-Boltzmann distribution

$$f_v(v_{||}) = \sqrt{\frac{m}{2\pi k_BT_{||}}}\exp\left[\frac{-m(v_{||}-u_\infty)^2}{2k_BT_{||}}\right], \tag{5.7}$$

which is a normal distribution within the moving frame of reference of the beam and then has a standard deviation $\sigma_v = \sqrt{k_BT_{||}/m}$. The speed ratio S can thus be calculated from the width of the speed distribution (which can be measured using the time-of-flight method - see

p_0 / bar	v / ms^{-1}	Δv / ms^{-1}	S /1	ΔS / 1
3	1865	10	10.5	0.2
6	1895	10	14	0.2
11	1927	10	16.8	0.1
16	1948	10	18.8	0.1
21	1961	10	20	0.1
26	1973	10	20.9	0.1
31	1981	10	21.9	0.1
51	2012	10	25.1	0.1
71	2027	10	27.1	0.2
91	2039	10	28.8	0.2
111	2050	10	30.4	0.2
131	2058	10	31.5	0.2
151	2065	11	32.9	0.2
171	2067	11	33.5	0.2

Table 5.1: Results from the time-of-flight measurements for a supersonic-expansion D_2 beam with T_0=310 K. p_0 is the stagnation pressure of the source, v is the measured terminal speed, Δv is the uncertainty in the speed measurement, S is the measured speed ratio, ΔS is the uncertainty in the speed-ratio measurement.

section 5.2.1). S is related to the full-width half-maximum (FWHM) of the speed distribution $\Delta v = 2\sqrt{2\ln(2)}\sigma_v$ and the mean value u_∞ of the velocity distribution by

$$S = 2\sqrt{\ln(2)}\frac{u_\infty}{\Delta v} \tag{5.8}$$

The model for the molecular deuterium expansion used in the paper estimates both u_∞ and $T_{||}$, which can thus be used to estimate the speed ratio of the beam using equation 5.6. The experimental speed-ratio results are summarized in tables 5.2 and 5.1.

5.1.4 Virtual source size

As mentioned before, the region where collisions between beam particles cease is called the quitting surface which spherically surrounds the source with the nozzle at the origin (see figure 5.1). Beyond the quitting surface the beam's particles follow straight trajectories. The particle velocities normal to the beam axis follow a Gaussian distribution, that corresponds to a so-called perpendicular temperature. The trajectories of the particles defined by this distribution can be traced back to a plane of least confusion that is perpendicular to the beam axis. This virtual source plane does not necessarily coincide with the plane containing the nozzle opening, but can be well approximated by it. The spatial distribution of the intersections of the trace-back particle trajectories with the virtual source plane constitutes the virtual source. Its width is therefore a measure of the perpendicular temperature of the beam.

Following the above definition the virtual source width w_s is related to the perpendicular beam

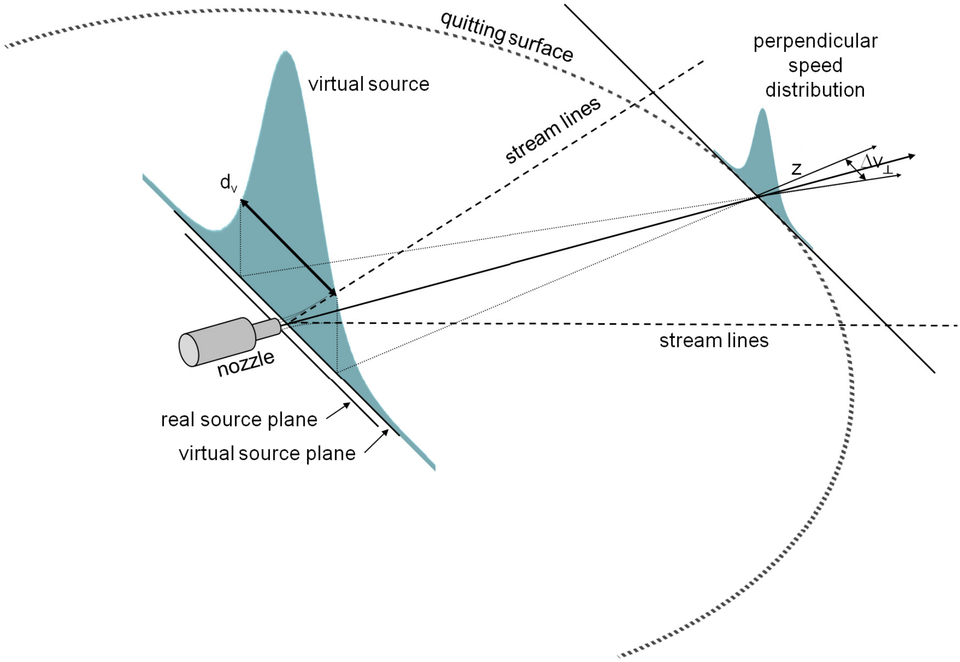

Figure 5.1: Schematic illustrating of the relation between the width of the virtual source and the perpendicular speed distribution. The gas exiting the nozzle initially is in a continuum flow regime that is symmetric about the z-axis. The stream lines of this flow are curved initially but become straight after a few nozzle diameters. Then they can be traced back to the so-called virtual-source point. During the expansion the density of the beam gas decreases and the mean-free-path increases. At the quitting surface collisions finally cease and the particles travel along straight trajectories thereafter. The trajectories at the quitting surface can be traced back and form a Gaussian spatial distribution in the virtual source plane. (after Reisinger et al [78])

p_0 / bar	v / ms^{-1}	Δv / ms^{-1}	S /1	ΔS / 1
3	1094	6	17	0.1
6	1107	6	20.2	0.1
11	1114	6	23.2	0.1
16	1118	6	24.8	0.1
21	1121	6	25.4	0.1
26	1121	6	24.3	0.1
31	1122	6	22.5	0.1
51	1126	6	20.9	0.1
71	1129	6	21.3	0.1
91	1132	6	21.7	0.1
111	1136	6	21.8	0.1
131	1141	6	22.1	0.1

Table 5.2: Results from the time-of-flight measurements for a supersonic-expansion D_2 beam with T_0=106 K. p_0 is the stagnation pressure of the source, v is the measured terminal speed, Δv is the uncertainty in the speed measurement, S is the measured speed ratio, ΔS is the uncertainty in the speed-ratio measurement.

temperature $T_\perp$ and the distance of the quitting surface from the nozzle D_{QS} by

$$w_s = 2\sqrt{2\ln 2}\;\frac{D_{QS}\quad\sqrt{k_B T_\perp / m}}{u_\infty} \tag{5.9}$$

m is the mass of the particle and u_∞ the terminal speed.

In paper E the virtual source is imaged with two different zone plates (one for each nozzle temperature). Taking into account the focusing properties of the zone plate (see section 5.2.2) the actual width of the virtual source can be extracted. The paper compares this virtual source width with the results from the theoretical model that predicts the perpendicular temperature, terminal speed and distance of the quitting surface.

5.1.5 Beam condensation

The model calculations correspond very well to the experimental values measured for the terminal speed, terminal speed ratio and the virtual-source width. The latter deviated by a factor of about 1.5. However, for the cold-nozzle beam (T_0=106 K) there is a clear deviation from the trend predicted by the model at increasing source pressures. This is explained by condensation effects in the source.

In order to further investigate the onset of clustering we recorded mass-spectra, by varying the magnetic field used to select a specific atomic mass in the electron-bombardment detector [80]. The mass-spectra are shown in figures 5.2 and 5.3. In these measurements a background signal measured with the beam off was subtracted. Unfortunately, this background signal due to the gas in the detector chamber was not very stable despite the fact that several were

p_0 / bar	w_{exp} / µm	Δw_{exp} / µm	w_{model} / µm	w_s / µm	Δw_s / µm
3	19.9	0.6	15.4	23.4	0.7
6	20.1	0.3	14.8	25.2	0.4
11	21.3	0.3	13.6	30.4	0.4
16	21.3	0.2	12.8	31.6	0.3
21	21.5	0.2	12.4	32.6	0.3
26	22	0.2	11.9	34.3	0.3
31	22.6	0.2	11.7	35.8	0.3
51	25.5	0.2	12.1	41.6	0.3
71	28.6	0.2	12.5	47.7	0.3
91	32.9	0.2	12.7	56.3	0.3
111	35.1	0.2	13.8	59.8	0.3
131	37.4	0.2	15.5	63.1	0.3
151	40.5	0.2	17.5	67.7	0.3
171	42.4	0.2	19.2	70.1	0.3

Table 5.3: Virtual-source width results from the zone-plate focusing measurements with a supersonic-expansion D_2 beam at T_0=310 K. p_0 is the stagnation pressure of the source, w_{exp} is the measured width of the focus, Δw_{exp} is the uncertainty in the focus-width measurement, w_{model} is the width of the focus from a point source (see section 5.2.2), w_s is the deconvoluted width of the virtual source taking into account the magnification of the image produced by the zone plate, Δw_s is the uncertainty in the virtual-source width. The latter does not take into account any uncertainty resulting from the deconvolution.

p_0 / bar	w_{exp} / µm	Δw_{exp} / µm	w_{model} / µm	w_s / µm	Δw_s / µm
3	16.9	0.2	15.06	14.7	0.2
6	17.5	0.1	13.89	20.4	0.1
11	19.7	0.1	13.11	28.2	0.1
16	20.9	0.1	12.71	31.8	0.2
21	23	0.2	12.47	37.0	0.3
26	27.5	0.2	12.52	46.9	0.3
31	35.6	0.2	12.61	63.8	0.4
51	59	0.5	12.61	110.4	0.9
71	69	2	12.46	130.0	3.8
91	81	4	12.32	153.4	7.6
111	88	2	12.22	167.0	3.8
131	100	4	12.13	190.2	7.6

Table 5.4: Virtual-source width results from the zone-plate focusing measurements with a supersonic-expansion D_2 beam at T_0=106 K. p_0 is the stagnation pressure of the source, w_{exp} is the measured width of the focus, Δw_{exp} is the uncertainty in the focus-width measurement, w_{model} is the width of the focus from a point source (see section 5.2.2), w_s is the deconvoluted width of the virtual source taking into account the magnification of the image produced by the zone plate, Δw_s is the uncertainty in the virtual-source width. The latter does not take into account any uncertainty resulting from the deconvolution.

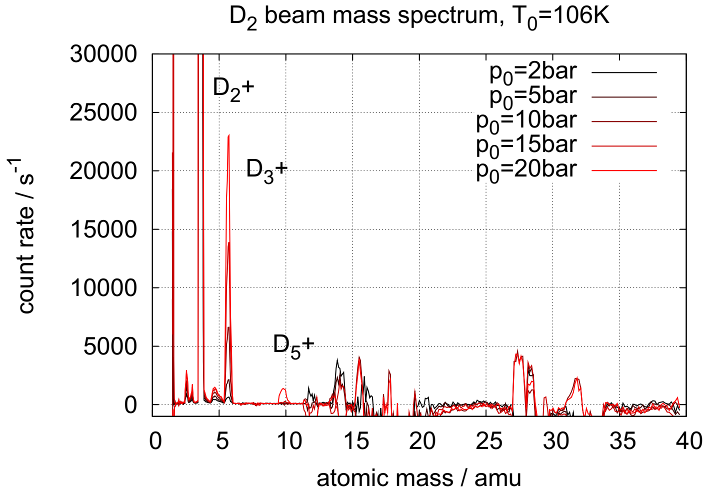

Figure 5.2: Mass spectrum of deuterium (D_2) beam at varying source pressure and T_0=106K. The count rate measured for the D_2+ peak is about 650000 s^{-1} at p_0=20 bar.

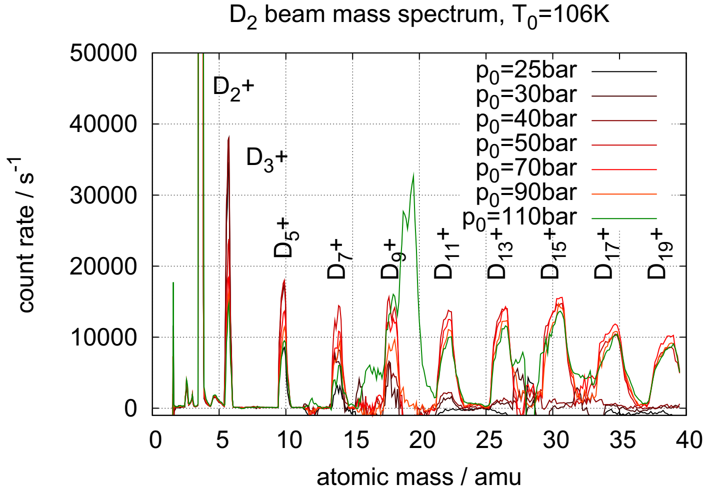

Figure 5.3: Mass spectrum of deuterium (D_2) beam at varying source pressure and T_0=106K. The count rate measured for the D_2+ peak is about 670000 s^{-1} at p_0=110 bar.

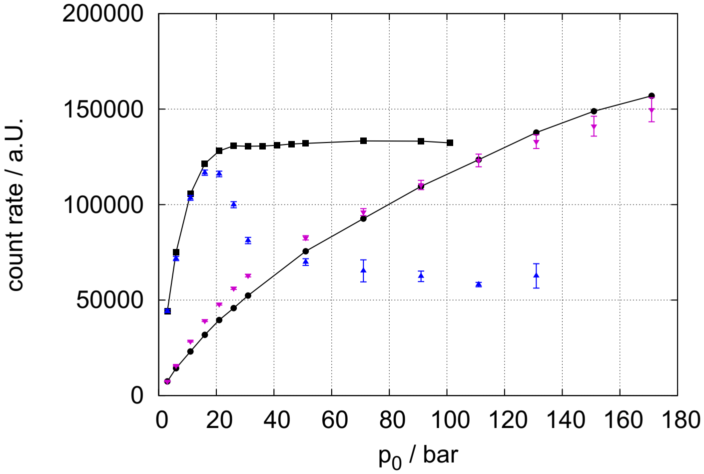

Figure 5.4: Zone plate used as cluster filter. The black lines give the 'D_2+' signal at the detector (■: T_0=106K; •: T_0=310K, scaled by a factor 1/10). The blue (▲: T_0=106K) and purple (▼: T_0=310K) data-sets are the scaled total intensities in the first order zone plate focus. In the case of the warm-nozzle beam the two signals approximately correspond to each other, while for the cold-nozzle beam the total intensity in the first order focus shows a clear discrepancy above a nozzle pressure ov about 16 bar. This shows that cluster-fragments contribute to the D_2+ signal at the detector.

recorded during the measurement of the mass-spectra. This explains the fluctuations especially at atomic masses 16,17 and 18 which correspond to water (H_2O) and its radicals produced in the electron bombardment detector.

Note that the observed peaks other than the mass-4 peak from the monomer correspond to odd-numbered atomic deuterium clusters. This is due to fragmentation of the clusters that occurs in the detector. Peaks corresponding to the even-numbered cluster-fragments can be observed as well, but are at least an order of magnitude less intense (not shown in figures 5.2 and 5.3). For a more detailed study of the clustering in a D_2 supersonic expansion please refer to Ekinci et al. [27].

In figure 5.4 I compare the total intensity in the first-order diffraction peak from the zone plate to the intensity of the beam without zone plate for both the cold and warm-nozzle beams. From section 3.1 it is clear that the focal length of the zone plate is inversely proportional to wavelength. The de-Broglie wavelength is inversely proportional to particle mass, and hence the imaging plane of the zone plate strongly depends on the cluster mass. Therefore the combination of the zone plate with the pinhole aperture at the detector act as an additional mass filter. Figure 5.4 thus clearly shows that the D_{2+} is not just due to monomers for the cold-nozzle beam. The real monomer count rate, which corresponds to the total intensity in the first diffraction order, has a peak at about 16 bar, then decreases and eventually stabilizes at pressures above about 50 bar. The behavior is very similar to the signals from the higher masses D_{3+} and D_{5+} which also exhibit a peak followed by a stabilization at a lower intensity (see figure 13 in paper E).

By considering the energy balance in equation 5.4 it is possible to associate a deviation of the beam parameters predicted by the model from the experimental values with cluster condensation since the model does not take condensation into account. The condensation process provides additional energy and heats the translational, random translational, perpendicular and rotational degrees of freedom. We have essentially measured the energy associated to each of them except for the energy associated with the rotational temperature of the beam, which we estimated instead. By assuming a value of $\Delta h_{lg\infty} = 1289.9\ J/mol$ for the specific heat of vaporization at the triple point for normal deuterium [59], it was possible to estimate the condensed fraction associated of the beam based the differences between model and experiment. However, the accuracy of this estimate is reduced by the fact that the model does not take into account the real gas properties, which might also be the source of deviations from the experimental data. Initial calculations with the real-gas thermodynamic properties of D_2 [73] indicate that especially the rise in terminal speed is in part due to the real-gas properties at higher nozzle-pressures.

5.2 Experimental aspects

This section documents how the parameters discussed in the previous section were deduced from the experimental data. The time-of-flight distribution needs to be corrected for systematic errors and the measurement of the width of the zone-plate focus is convoluted with the point-spread function of the zone plate.

5.2.1 Calibration of time-of-flight measurements

The parallel speed distribution of the beam was measured using the time-of-flight setup of the supersonic expansion apparatus as described in paper E and section 5.2.1.

In order to be able to estimate the real energy distribution of the beam from the measured time-of-flight (TOF) distribution a number of factors need to be taken into account. The parameters used to calibrate the data in Paper E are summarized in table 5.5.

The actual most probable TOF t_f (the peak of the real TOF distribution) is given by

$$t_f = t_d + t_p - t_c - t_{ch}/2 \tag{5.10}$$

where t_d is the delay time that the electronics waits after each trigger signal from the chopper. t_p is the peak time recorded in the measurement. t_c is a correction time that takes into account any misalignment between the actual intersection time of the slit with the beam and the photoelectric barrier that sends the trigger signal. t_{ch} is the width of the time channels used in the time-resolved measurement. This correction ensures that each data point is associated with the middle of this time interval.

While t_d and t_{ch} are parameters that are set before the experiment and t_p can be extracted from the data, t_c needs to be determined in a calibration experiment. This experiment merely

L_{CD} at L_D=580 mm	(2010±10) mm
r_{ch} at y_{ch}=1.020 inch	(68.3±0.5) mm
w_{ch} at y_{ch}=1.020 inch	(1.19±0.05) mm
ν_{ch}	(275±1) Hz
X_D	(4.6±0.5) mm
α	(9.7±0.3)

Table 5.5: Parameters for the evaluation and calibration of TOF data sets. L_{CD} is the distance between chopper and detector, L_D is the absolute position of the detector on the detector arm, r_{ch} is the distance between the rotation center of the chopper and the position in the slit where the beam passes, y_{ch} is the absolute position of chopper, w_{ch} is the chopper slit width, ν_{ch} is the rotational frequency of the chopper, X_D α is the length along which particles are ionized in the detector, α is the calibration constant evaluated in figure 5.5.

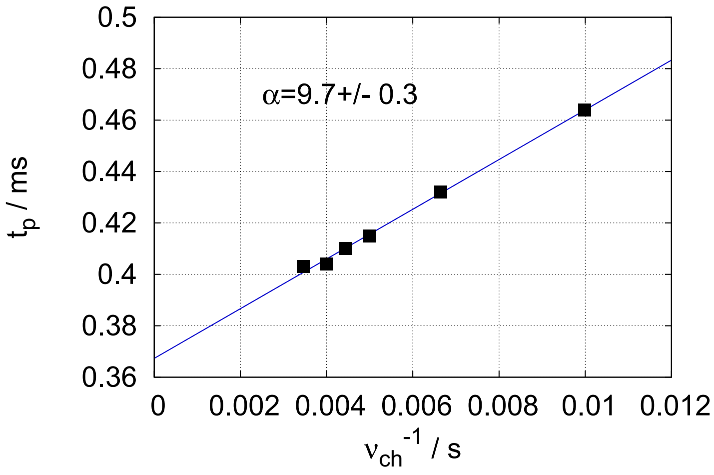

Figure 5.5: Calibration of chopper correction time t_c. The frequency of the chopper ν_{ch} is changed for constant beam conditions and the peak time t_p extracted from the recorded TOF distributions. The slope of the fitted straight line gives the required correction factor α. The slight deviation of the high frequency measurement points are due to variations in the nozzle temperature (This data-set was recorded with p_0=30 bar and T_0=106 K).

consists of keeping the beam parameters constant and changing the frequency of the chopper. As the chopper frequency ν_{ch} tends to infinity the correction time should reduce to zero. So in general we can use the correction factor α defined in the following equation to correct each peak time:

$$t_c = \alpha \, \frac{1}{\nu_{ch}} \tag{5.11}$$

α is determined in a linear fit to the peak times t_p as a function of $1/\nu_{ch}$ as shown in figure 5.5. Note that this calibration experiment needs to be done every time the beam-path is changed in some way, for example by moving one of the apertures or exchanging the skimmer. The most probable speed of the beam can thus be calculated by $v = L_{CD}/t_f$.

In addition to the shift of the peak time the width of the TOF distribution is also affected by systematic errors in the experiment. When the beam packages start their flight at the chopper they already have a finite width determined by the chopper slit-width w_{ch}, the rotational frequency ν_{ch} of the chopper and the radius of the slit position that is used to chop the beam r_{ch}. Furthermore, when the beam packages arrive at the detector they are not detected at an infinitely small region but they are ionized over a certain distance X_D. Assuming that each of these contributions to the measured distribution width is Gaussian we can estimate the actual width of the speed distribution Δt_f by

$$\Delta t_f^2 = \Delta t_g^2 - \Delta t_C^2 - \Delta t_D^2 \tag{5.12}$$

where Δt_g is the measured full-width at half-maximum (FWHM) of the TOF distribution. Δt_C is the FWHM of the distribution due to the finite chopper opening and Δt_D is the FWHM of the distribution due to the finite detection length. The broadening due to the detector can be estimated as follows

$$\Delta t_D = \frac{X_D}{v} \tag{5.13}$$

where v is the speed calculated above. The broadening due to the chopper is approximately given by:

$$\Delta t_C = \frac{w_{ch}}{2 * \pi \, r_{ch} \, \nu_{ch}} \tag{5.14}$$

The speed ratio of the beam can thus be estimated by $S = 2\sqrt{\ln(2)}\; t_f/\Delta t_f$. Note that Δt_C is generally the larger of the two, so that it is the most important especially when determining large speed ratios. Further it is important to ensure that the width of the beam (which is determined by the skimmer and the aperture limiting the beam's cross-section on the way to the detector) is about the same as the chopper width. Otherwise the broadening function cannot be estimated by a Gaussian and equation 5.12 is not accurate.

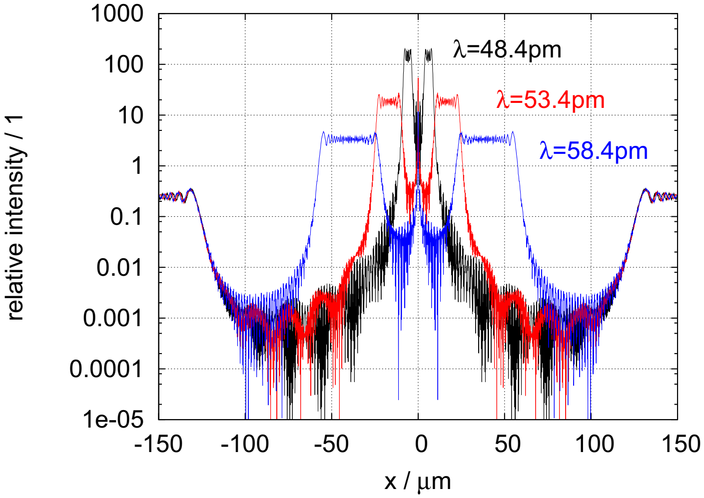

Figure 5.6: In this figure the calculated lateral relative intensity of the point-source diffraction pattern in the imaging plane for three different wavelengths is shown. Note the logarithmic scale on the y-axis. The zeroth diffraction can be seen at a distance greater than about 120 µm from the central axis and has the expected relative intensity of 0.25 on average. The first order focus includes a shadow due to the central stopping disc of the zone plate. On the central axis one can notice a Poisson spot. For the focus model we calculated a diffraction pattern of this type every 0.1 pm in the wavelength ranges 43.4 pm - 65.6 pm (warm nozzle) and 82.8 pm - 106.8 pm (cold nozzle).

5.2.2 Zone-plate focusing

The position of the focal plane of the zone-plate depends on the de-Broglie wavelength of the beam. The wavelength of the beam is mainly determined by the source temperature T_0, but also changes as a function of source pressure p_0. The position of the plane in which the beam was detected was kept constant in the experiment. Therefore, the measured focus width will be slightly wider than it would be in the ideal focal plane. Furthermore, the D_2 beam has a relatively broad speed distribution which also results in a broadening of the focus. The focus is also a magnified image of the virtual source (see section 3.1). The virtual source FWHM w_s is hence calculated from the FWHM of the focus using the equation

$$w_s = \frac{g}{b} \cdot \sqrt{w_{exp}^2 - w_{model}^2} \tag{5.15}$$

where w_{exp} is the measured FWHM of the focus and w_{model} is the FWHM of the point-spread function for the measured wavelength distributions.

The point-spread function (PSF) of the zone plate was calculated using an extended version of the diffraction simulation described in section 2.2. For each point in the image plane the calculated phasors from every transparent zone are summed taking their relative phases into account to give the diffraction image of the full zone plate. This was done for a large number of different wavelengths determined from the measured wavelength distributions (TOF distribution). The lateral relative intensities are shown in figure 5.6 for three different wavelengths.

The resulting diffraction images were summed incoherently scaling the intensity according to the wavelength distribution. Finally, the resulting diffraction image was convoluted with the aperture function of the pinhole that was used to scan the images (11-µm in diameter). The FWHM of the resulting point-spread function was determined by fitting a Gaussian function.

5.3 Discussion

In this chapter which is related to paper E the supersonic expansion of normal D_2 was investigated with time-of-flight methods and by imaging the virtual source with a free-standing Fresnel zone plate. The three parameters terminal speed, terminal speed ratio and virtual source width of the expansion were measured and compared to a theoretical model. The theoretical model predicts the parallel speed, parallel and perpendicular temperature as well as the rotational temperature of the beam at the quitting surface. This it achieves by assuming axial symmetry and solving the Boltzmann equation along the central stream line. The measured virtual-source widths were deconvoluted using the point-spread function of the zone plate which was calculated in the fixed imaging plane for each measured wavelength distribution.

The experimental data were collected for two different source temperatures, namely T_0=106 K and T_0=310 K, using a nozzle of 10 µm diameter. The source pressures were varied in the range of p_0=3-171 bar for the warm-nozzle beam and p_0=3-131 bar for the cold-nozzle beam. Both measured terminal speed and terminal speed ratio corresponded well to the model, except for where condensation effects were significant (cold-nozzle and pressures above about 21 bar). The model over-estimated the virtual-source width by about a factor of 1.5. Virtual source widths were in the range (14.7±0.5) µm to (190.2±0.5) µm for the cold-nozzle beam and from (23.4±0.5) µm to (70.1±0.5) µm for the warm-nozzle beam.

Based on the deviation of the experimental data from the model it was possible to estimate the fraction of condensed molecules in the beam. We also showed using the zone plate as a de-Broglie monochromator (molecular-mass selector) that the mass-4 signal is partially due to cluster fragments produced in the electron-bombardment detector at higher stagnation pressures.

In the future it might be possible to fabricate zone plates that correspond to the different cluster masses and thus determine accurately cluster size distributions in supersonic expansions. Such zone plates might be additionally useful in applications where it is advantageous to work with a particular cluster mass.

Furthermore, inital calculations have shown that it is important to take into account the real gas properties of deuterium especially at the higher stagnation pressures. This might lead to an overall accurate theoretical description of the D_2 supersonic expansion.

Chapter 6

Conclusion and outlook

This final chapter summarizes the results from the five articles presented in this thesis. Additionally, possible future developments in each of the discussed applications of matter-wave diffraction are outlined.

6.1 Poisson's spot with molecules

A Poisson-spot experiment has been performed with a supersonic-expansion molecular deuterium beam (Paper A). The diffraction pattern was recorded at three different distances behind the circular free-standing disc and compared to Fresnel diffraction theory. To get a good correspondence between data and model the edge-roughness of the circular disc had to be taken into account.

In paper B the Fresnel diffraction model was modified to take into account van-der-Waals interaction with the circular disc-edge and compared to a classical particle deflection model. It was found that it is possible to distinguish between particle and wave behavior by studying the dependence of the diffraction pattern on edge-roughness of the circular obstacle. It was also determined that a Poisson-spot experiment with C70 molecules would be very challenging with current methods.

The Poisson-spot experiment may yet be interesting for studying the wave-nature of large molecules, by examining the diffraction pattern behind many circular obstacles at the same time. Another interesting future application could be the study of long-range particle-wall interactions. By appropriately patterning the edge-corrugation of the disc the effect from diffraction could be completely canceled so that any on-axis signal would be due to interaction with the disc-edge.

6.2 Neutral helium microscopy

Another interesting application of matter-wave diffraction is the focusing of supersonic-expansion beams and using them in this way for microscopy. The low energy and neutrality of such beams make them an ideal probe for sensitive and insulating materials. Paper C looked at using free-standing Fresnel zone-plates to focus a neutral helium beam. Two transmission images of a carbon foil with 2-µm-diameter holes were presented which had state-of-the-art resolution. In addition the paper demonstrates the focusing of a molecular (deuterium) supersonic-beam to highlight other possible applications such as for example the possibility to measure the permeability of membranes in a spatially resolved fashion.

The paper further estimates that the minimal usable focus that can be formed with free-standing zone-plates is about 300 nm with currently available techniques. In the future it might be possible to do better by combining the amplitude zone-plates with other types of atom lenses (electric or magnetic). An option to increase the efficiency of the zone-plates, which is currently about 10 %, might be to fabricate phase-shift zone-plates based on the phase-shift imposed on the beam atoms by the van-der-Waals interaction with the grating wall.

Nevertheless, the main challenge in neutral-helium microscopy remains detector efficiency. The study of efficient detection mechanisms will be imperative on the road to reflection neutral-atom-microscopy.

6.3 Fabrication of free-standing zone-plates

Paper D describes the fabrication of free-standing Fresnel zone-plates from silicon-nitride membranes. The process uses electron-beam lithography and reactive ion-etching to pattern the membranes. A number of zone plates have been fabricated for focusing both room temperature and cold-nozzle supersonic expansion beams of atomic mass 4 (i.e. helium or molecular deuterium) on two different setups. The zone-plates were tested with a ground-state helium beam and were found to have close to the theoretical transmission properties.

Pattern-placement errors that occur during the electron-beam lithography step were found to affect the diffraction efficiency of at least the large multi-writefield zone plate. Such patterning errors can be tackled by supplying a precise reference grid that the patterns can be aligned to. Chapter 4 describes the fabrication of such reference grids, and how they can be used to minimize both inter- and intra-writefield distortion in electron-beam lithography.

In the future it should be possible to demonstrate the aforementioned pattern correction techniques by using third-order zone-plate diffraction which is more sensitive to the fidelity of the zone-plate pattern. In addition it will be interesting to attempt fabrication of phase-shift zone-plates or combined atom lenses as mentioned in the previous section. Furthermore, composite zone-plates that combine first- and third-order diffraction will be fabricated to supply enough intensity for reflection neutral-atom microscopy.

6.4 Characterization of supersonic expansions

Supersonic-expansions are an important tool in surface science and other fields. For this reason it is useful to study their properties and create models that can predict them. In paper E we used a Fresnel zone-plate to image the virtual source of a deuterium supersonic expansion and thus determine its width which is a measure of the perpendicular temperature of the beam. In addition the energy distribution parallel to the beam axis was measured with conventional time-of-flight methods.

The experimental data were compared to a simple model that simulates the expansion by numerically solving the Boltzmann equation. It was found to be in good agreement with experiment, and any deviations could be explained by condensation effects. Based on this deviation it was possible to estimate the fraction of condensed molecules in the beam.

In addition we showed that the Fresnel zone-plate can be used to filter out clusters due to the zone-plate's strong chromatic aberration. In the future this might be used to create beams of a specific cluster mass.